NRC·CNRC

NRC Publications Archive
Archives des publications du CNRC

The Next Generation Virgo Cluster Survey. XXXIV. Ultracompact dwarf galaxies in the Virgo cluster

Liu, Chengze; Côté, Patrick; Peng, Eric W.; Roediger, Joel; Zhang, Hongxin; Ferrarese, Laura; Sánchez-Janssen, Ruben; Guhathakurta, Puragra; Yang, Xiaohu; Jing, Yipeng; Alamo-Martínez, Karla; Blakeslee, John P.; Boselli, Alessandro; Cuilandre, Jean-Charles; Duc, Pierre-Alain; Durrell, Patrick; Gwyn, Stephen; Jordán, Andres; Ko, Youkyung; Lançon, Ariane; Lim, Sungsoon; Longobardi, Alessia; Mei, Simona; Mihos, J. Christopher; Muñoz, Roberto; Powalka, Mathieu; Puzia, Thomas; Spengler, Chelsea; Toloba, Elisa

This publication could be one of several versions: author's original, accepted manuscript or the publisher's version. / La version de cette publication peut être l'une des suivantes : la version prépublication de l'auteur, la version acceptée du manuscrit ou la version de l'éditeur.
For the publisher's version, please access the DOI link below./ Pour consulter la version de l'éditeur, utilisez le lien DOI ci-dessous.

Publisher's version / Version de l'éditeur:
https://doi.org/10.3847/1538-4365/abad91
The Astrophysical Journal Supplement Series, 250, 1, 2020-09-10

NRC Publications Archive Record / Notice des Archives des publications du CNRC :
https://nrc-publications.canada.ca/eng/view/object/?id=af0146a7-32d3-422a-9c57-8f54436cee33
https://publications-cnrc.canada.ca/fra/voir/objet/?id=af0146a7-32d3-422a-9c57-8f54436cee33

Access and use of this website and the material on it are subject to the Terms and Conditions set forth at
https://nrc-publications.canada.ca/eng/copyright
READ THESE TERMS AND CONDITIONS CAREFULLY BEFORE USING THIS WEBSITE.

L'accès à ce site Web et l'utilisation de son contenu sont assujettis aux conditions présentées dans le site
https://publications-cnrc.canada.ca/fra/droits
LISEZ CES CONDITIONS ATTENTIVEMENT AVANT D'UTILISER CE SITE WEB.

Questions? Contact the NRC Publications Archive team at PublicationsArchive-ArchivesPublications@nrc-cnrc.gc.ca. If you wish to email the authors directly, please see the first page of the publication for their contact information.

Vous avez des questions? Nous pouvons vous aider. Pour communiquer directement avec un auteur, consultez la première page de la revue dans laquelle son article a été publié afin de trouver ses coordonnées. Si vous n'arrivez pas à les repérer, communiquez avec nous à PublicationsArchive-ArchivesPublications@nrc-cnrc.gc.ca.

National Research Council Canada | Conseil national de recherches Canada

Canada

The Astrophysical Journal Supplement Series, 250:17 (28pp), 2020 September https://doi.org/10.3847/1538-4365/abad91
© 2020. The Author(s). Published by the American Astronomical Society.
OPEN ACCESS

The Next Generation Virgo Cluster Survey. XXXIV. Ultracompact Dwarf Galaxies in the Virgo Cluster

Chengze Liu[1], Patrick Côté[2], Eric W. Peng[3,4], Joel Roediger[2], Hongxin Zhang[5,6], Laura Ferrarese[2], Ruben Sánchez-Janssen[7], Puragra Guhathakurta[8], Xiaohu Yang[1], Yipeng Jing[1], Karla Alamo-Martínez[9], John P. Blakeslee[2], Alessandro Boselli[10], Jean-Charles Cuilandre[11], Pierre-Alain Duc[12], Patrick Durrell[13], Stephen Gwyn[2], Andres Jordán[14,15], Youkyung Ko[3], Ariane Lançon[12], Sungsoon Lim[2,16], Alessia Longobardi[10], Simona Mei[17,18], J. Christopher Mihos[19], Roberto Muñoz[9], Mathieu Powalka[12], Thomas Puzia[9], Chelsea Spengler[2], and Elisa Toloba[20]

[1] Department of Astronomy, School of Physics and Astronomy, and Shanghai Key Laboratory for Particle Physics and Cosmology, Shanghai Jiao Tong University, Shanghai 200240, People's Republic of China; czliu@sjtu.edu.cn
[2] Herzberg Astronomy and Astrophysics Research Centre, National Research Council of Canada, 5071 W. Saanich Road, Victoria, BC, V9E 2E7, Canada
[3] Department of Astronomy, Peking University, Beijing 100871, People's Republic of China
[4] Kavli Institute for Astronomy and Astrophysics, Peking University, Beijing 100871, People's Republic of China
[5] School of Astronomy and Space Science, University of Science and Technology of China, Hefei 230026, People's Republic of China
[6] CAS Key Laboratory for Research in Galaxies and Cosmology, Department of Astronomy, University of Science and Technology of China, Hefei, Anhui 230026, People's Republic of China
[7] STFC UK Astronomy Technology Centre, Royal Observatory, Blackford Hill, Edinburgh, EH9 3HJ, UK
[8] UCO/Lick Observatory, Department of Astronomy and Astrophysics, University of California Santa Cruz, 1156 High Street, Santa Cruz, CA 95064, USA
[9] Instituto de Astrofísica, Pontificia Universidad Católica de Chile, Av. Vicuña Mackenna 4860, 7820436 Macul, Santiago, Chile
[10] Aix-Marseille Univ, CNRS, CNES, LAM, Marseille, France
[11] AIM Paris Saclay, CNRS/INSU, CEA/Irfu, Université Paris Diderot, Orme des Merisiers, F-91191 Gif-sur-Yvette Cedex, France
[12] Université de Strasbourg, CNRS, Observatoire astronomique de Strasbourg, UMR 7550, F-67000 Strasbourg, France
[13] Department of Physics and Astronomy, Youngstown State University, Youngstown, OH 44555, USA
[14] Facultad de Ingeniería y Ciencias, Universidad Adolfo Ibáñez, Av. Diagonal las Torres 2640, Peñalolén, Santiago, Chile
[15] Millennium Institute for Astrophysics, Chile
[16] University of Tampa, 401 West Kennedy Boulevard, Tampa, FL 33606, USA
[17] Université de Paris, F-75013, Paris, France, LERMA, Observatoire de Paris, PSL Research University, CNRS, Sorbonne Université, F-75014 Paris, France
[18] Jet Propulsion Laboratory and Cahill Center for Astronomy & Astrophysics, California Institute of Technology, 4800 Oak Grove Drive, Pasadena, California 91011, USA
[19] Department of Astronomy, Case Western Reserve University, 10900 Euclid Avenue, Cleveland, OH 44106, USA
[20] Department of Physics, University of the Pacific, 3601 Pacific Avenue, Stockton, CA 95211, USA
Received 2020 January 29; revised 2020 July 25; accepted 2020 July 27; published 2020 September 10

Abstract

We present a study of ultracompact dwarf (UCD) galaxies in the Virgo cluster based mainly on imaging from the Next Generation Virgo Cluster Survey (NGVS). Using ∼100 deg^2 of u^*giz imaging, we have identified more than 600 candidate UCDs, from the core of Virgo out to its virial radius. Candidates have been selected through a combination of magnitudes, ellipticities, colors, surface brightnesses, half-light radii, and, when available, radial velocities. Candidates were also visually validated from deep NGVS images. Subsamples of varying completeness and purity have been defined to explore the properties of UCDs and compare to those of globular clusters and the nuclei of dwarf galaxies with the aim of delineating the nature and origins of UCDs. From a surface density map, we find the UCDs to be mostly concentrated within Virgo's main subclusters, around its brightest galaxies. We identify several subsamples of UCDs—i.e., the brightest, largest, and those with the most pronounced and/or asymmetric envelopes—that could hold clues to the origin of UCDs and possible evolutionary links with dwarf nuclei. We find some evidence for such a connection from the existence of diffuse envelopes around some UCDs and comparisons of radial distributions of UCDs and nucleated galaxies within the cluster.

Unified Astronomy Thesaurus concepts: Ultracompact dwarf galaxies (1734); Globular star clusters (656); Galaxy nuclei (609); Dwarf elliptical galaxies (415); Virgo Cluster (1772); Galaxy formation (595)

Supporting material: machine-readable tables

1. Introduction

Roughly two decades ago, investigators reported the discovery of a potentially new class of stellar system in the Fornax cluster (Hilker et al. 1999; Drinkwater et al. 2000; Phillipps et al. 2001). These systems appeared to bridge the gap between normal globular clusters (GCs) and early-type galaxies (including the subset of compact elliptical galaxies) and so were named ultracompact dwarf galaxies (UCDs). Since then, such objects have been identified around field galaxies (e.g., Norris & Kannappan 2011; Jennings et al. 2014) as well as in galaxy groups and clusters: i.e., Virgo (Haşegan et al. 2005; Jones et al. 2006), A1689 (Mieske et al. 2005), Centaurus (Mieske et al. 2007a), Hydra (Wehner & Harris 2007), AS0740 (Blakeslee & Barber DeGraaff 2008), Coma (Madrid et al. 2010), the NGC 1023 group (Mieske et al. 2007b), the Dorado group (Evstigneeva et al. 2007a), the NGC 5044 group

Original content from this work may be used under the terms of the Creative Commons Attribution 4.0 licence. Any further distribution of this work must maintain attribution to the author(s) and the title of the work, journal citation and DOI.

(Faifer et al. 2017), the NGC 3613 group (De Bórtoli et al. 2020), and the NGC 1132 fossil group (Madrid 2011). While UCDs have luminosities comparable to faint dwarf elliptical (dE) galaxies, their sizes (∼10–100 pc) are smaller than "normal" dEs and yet larger than typical GCs. Due to their compact sizes and high stellar densities, they pose significant challenges for standard models of dwarf galaxy formation (see, e.g., Strader et al. 2013).

UCD formation models, which remain mostly qualitative in nature, generally invoke one of two basic scenarios. The first posits that UCDs may simply be the most massive members of the GC population, associated with the high-luminosity tail of the GC luminosity function (GCLF; e.g., Mieske et al. 2002) or possibly arising through mergers of massive star clusters (e.g., Fellhauer & Kroupa 2002). The second asserts that UCDs are the surviving nuclear star clusters of nucleated dwarf elliptical galaxies (dE, Ns) whose surrounding low-surface-brightness envelopes were removed via tidal stripping (e.g., Bekki et al. 2001). Of course, it is entirely possible that UCDs are not a monolithic population, i.e., that they are manifested through both scenarios (Haşegan et al. 2005; Hilker 2006; Mieske et al. 2006; Da Rocha et al. 2011).

In recent years, evidence has mounted in favor of a tidal stripping origin for at least some of these objects. The strongest evidence arguably comes from studies of the internal kinematics of UCDs: analyses of their integrated light show that UCDs can have high dynamical-to-stellar mass ratios (Forbes et al. 2014; Janz et al. 2015), while adaptive optics (AO) assisted integral-field unit (IFU) spectroscopy has enabled the discovery of supermassive black holes (SMBHs) in several systems (Seth et al. 2014; Ahn et al. 2017, 2018; Afanasiev et al. 2018). Concurrently, a kinematic study of the UCD population around M87 has shown that they follow radially biased orbits (Zhang et al. 2015). Meanwhile, photometric studies have revealed the presence of UCDs with asymmetric/tidal features (e.g., Jennings et al. 2015; Mihos et al. 2015; Voggel et al. 2016; Schweizer et al. 2018); UCDs with diffuse envelopes, which populate an apparent sequence in strength from dE, N to UCD (e.g., Drinkwater et al. 2003; Haşegan et al. 2005; Penny et al. 2014; Liu et al. 2015a); and clustering of GCs around UCDs (Voggel et al. 2016). With regard to stellar contents, investigators have found color–magnitude and mass–metallicity relations (e.g., Côté et al. 2006; Brodie et al. 2011; Zhang et al. 2018), the absence of color gradients (Liu et al. 2015a), and similarities in stellar populations to nuclei (e.g., Paudel et al. 2010; Janz et al. 2016). Additionally, *N*-body simulations and semianalytic models have demonstrated the viability of tidal stripping (within a cosmological framework) to transform dE, Ns to UCDs (e.g., Bekki et al. 2003; Pfeffer & Baumgardt 2013; Pfeffer et al. 2014, 2016; R. J. Mayes et al. 2020, in preparation). From this it seems clear that at least some portion of the population (e.g., massive UCDs) represent the stripped remnants of nucleated dwarf galaxies.

A prerequisite for the development and testing of any quantitative UCD formation model is reliable data on the physical properties of these objects, drawn from surveys with well-understood selection functions. Such data have proved elusive, however, and existing UCD samples are usually built from heterogeneous programs. Although they have been seen across a wide range of environments, most UCDs are located in groups and clusters, or associated with massive galaxies (e.g., Liu et al. 2015a). As the richest concentration of galaxies near the Milky Way (MW), the Virgo cluster is an ideal environment for a comprehensive UCD survey. A handful of systems were first discovered in Virgo by Haşegan et al. (2005) through a combination of Keck spectroscopy and Hubble Space Telescope (HST) imaging from the Advanced Camera for Surveys (ACS) Virgo Cluster Survey (Côté et al. 2004). Additional UCDs were later found in both imaging and/or spectroscopic programs (e.g., Jones et al. 2006; Chilingarian & Mamon 2008; Brodie et al. 2011; Strader et al. 2013; Liu et al. 2015a, 2015b; Sandoval et al. 2015; Zhang et al. 2015; Ko et al. 2017). These studies have tended to focus on UCDs associated with M87 or a few of the other brightest galaxies in Virgo. Currently, the largest UCD sample in this cluster contains ∼150 objects, spread over the M87, M49, and M60 regions (Liu et al. 2015a).

Given its enormous extent on the sky, a wide-field imaging survey is essential for building a homogeneous and complete sample of Virgo UCDs. The Next Generation Virgo cluster Survey (NGVS; Ferrarese et al. 2012) is a deep, multiband (u^*griz) imaging campaign of the Virgo cluster carried out with the MegaCam instrument on the Canada–France–Hawaii Telescope (CFHT). The survey covers an area of 104 deg^2 and is typified by excellent image quality, with a median FWHM of $0\farcs54$ in the i band (see their Figure 8). In principle, we can use these NGVS images to measure half-light radii for all compact Virgo objects brighter than $g \sim 21.5$ mag and larger than $r_h \sim 10$ pc (see Liu et al. 2015a), potentially producing the largest and most complete sample of UCDs in any environment. The analysis presented here builds on previous NGVS papers that have focused on the photometric and kinematic properties of UCDs (e.g., Liu et al. 2015a, 2015b; Zhang et al. 2015). It also complements other papers in the NGVS series dealing with other stellar systems in Virgo, including globular clusters (i.e., Durrell et al. 2014; Powalka et al. 2016a; Longobardi et al. 2018), galaxies (Guérou et al. 2015; Ferrarese et al. 2016, 2020; Sánchez-Janssen et al. 2016; Roediger et al. 2017), and their nuclei (i.e., Spengler et al. 2017; Sánchez-Janssen et al. 2019).

This paper is structured as follows. In Section 2 we provide an overview of the NGVS and the data products used in our analysis, while Section 3 describes the methodology we have used to identify UCD candidates. In Section 4 we present our results, including a new catalog of UCD candidates, and draw attention to a number of particularly interesting subsamples therein. We discuss these findings in Section 5, and in Section 6, summarize our conclusions and outline directions for future work. Throughout this study, we adopt a common distance to all UCDs (16.5 Mpc Mei et al. 2007; Blakeslee et al. 2009), corresponding to a distance modulus of $(m - M) = 31.09$ and physical scale of 80 pc arcsec^{-1}.

2. Data

2.1. Overview

The primary source of data used in this study is the NGVS. The survey footprint covers the two main subclusters of Virgo (A and B, centered on M87 and M49, respectively) out to their virial radii (i.e., $R_{200} = 5\fdg38$ for Virgo A and $3\fdg33$ for Virgo B). As described in Muñoz et al. (2014) and Liu et al. (2015a), the NGVS is an ideal resource for the study of compact stellar systems, e.g., GCs, UCDs, and dwarf nuclei. The NGVS

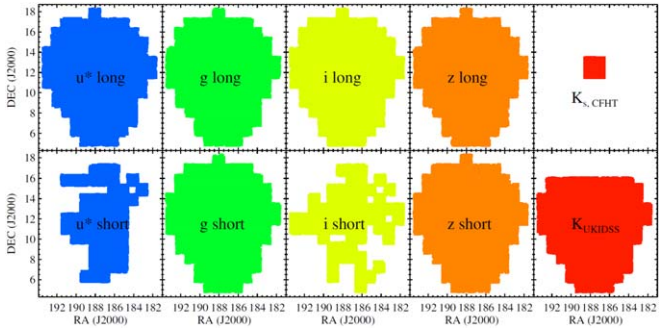

Figure 1. The areal coverage of our optical and near-infrared imaging, organized by exposure length (top: long, bottom: short). The NGVS achieved 100% completeness for the long exposures in the u^*giz bands and in the gz bands for the short exposures; short exposures in the u^*i bands were only partially completed. The NGVS-IR (K_s band; Muñoz et al. 2014) imaging only covers the center of subcluster A, while the UKIDSS (K band; Lawrence et al. 2007) data cover most of the NGVS footprint.

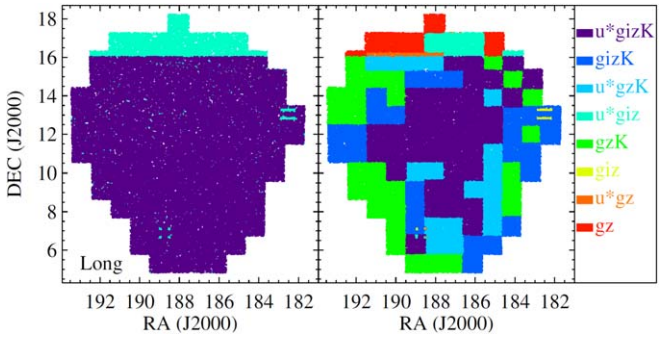

Figure 2. Summary of the spatial dependence of the multiwavelength photometry used to select UCDs, divided by exposure length (left: long-exposure catalog, right: short-exposure catalog).

imaging consists of short and long exposures, where the former can be used to find UCDs brighter than $g \sim 18.5$ mag. Such objects are interesting given that they define the extremes of UCD formation (and, in some cases, even host SMBHs; Seth et al. 2014; Ahn et al. 2018).

Figure 1 shows the final observing status of the NGVS, organized by exposure length. We have excluded the r band as those observations had to be partially sacrificed due to CFHT's dome shutter failure in 2012A. For the long exposures, the survey is fully complete in the remaining bands, while only partial areal coverage was achieved for the short exposures in the u^* (∼50% completeness) and i (∼57% completeness) bands.

Near-infrared imaging has proven to be a powerful tool for UCD selection (Muñoz et al. 2014; Liu et al. 2015a). As shown in the upper-right corner of Figure 1, we have deep K_s-band images in the central 4 deg^2 of subcluster A (NGVS-IR; Muñoz et al. 2014), which we have previously used to select a high-purity UCD sample around M87 (Liu et al. 2015a). Alternatively, as shown in the bottom-right panel of Figure 1, K-band imaging from UKIRT Infrared Deep Sky Survey (UKIDSS; Lawrence et al. 2007) covers a large fraction of the NGVS footprint. About ∼70% of the bright objects ($g_0 <$ 21.5 mag, where g_0 is the aperture-corrected magnitude measured within a 16 pixel diameter (∼3″) and corrected for Galactic extinction) in the NGVS have counterparts in the UKIDSS K band. Thus, although UKIDSS is much shallower than the NGVS-IR (5σ limiting magnitude ∼18.4 and ∼24.4 mag, respectively), it is nonetheless useful for separating UCDs from background galaxies (BGs) among the bright objects.

We summarize the combinations of imaging data at hand, separated by exposure length, in Figure 2. For the case of the long exposures (left panel), the footprint is simply divided into two areas depending on the availability of UKIDSS K-band imaging. The short-exposure map (right panel) is much more complicated owing to the incompleteness in the associated u^*- and i-band imaging.

Full details on the reduction of NGVS images can be found in Ferrarese et al. (2012). To generate a homogeneous catalog of compact objects, we run SExtractor (Bertin & Arnouts 1996) in double-image mode. We detect objects in the g band and then measure a set of parameters, including aperture magnitudes, in the u^*giz bands. In this study, we measure the luminosity and color of all detected objects with aperture magnitudes. To minimize systematics, we apply aperture corrections that account for point-spread function (PSF) variations within, and between, fields. Specifically, we use corrected 3.″0 diameter aperture magnitudes to represent total magnitudes and corrected 1.″5 diameter aperture magnitudes to estimate colors.

For the catalog generation and magnitude correction, we follow the method of Liu et al. (2015a), with one exception. Liu et al. (2015a) subtracted models of the diffuse light from nearby massive galaxies (M87, M49, and M60), whereas this is avoided in the current analysis to have a homogeneous catalog. We generate independent catalogs based on the short- and long-exposure images and then merge them into one afterwards. We adopt measurements from the short-exposure catalog for those objects that are saturated in the long exposures; otherwise, measurements are taken from the long-exposure catalog.

In addition to the imaging that forms the basis of this study, there are many past spectroscopic programs targeting the Virgo cluster that we can draw upon. Ferrarese et al. (2012) summarized the relevant programs for Virgo compact stellar systems (i.e., GCs, UCDs, and dE, Ns) as of 2012; these include radial velocity measurements from various Multiple Mirror Telescope (MMT)/Hectospec, Magellan/IMACS, Very Large Telescope/VIMOS, and Anglo-Australian Telescope (AAT)/AAOmega programs (see the paper for details). Since then, a number of NGVS-motivated spectroscopic programs have been undertaken (see, e.g., Zhang et al. 2015, 2018; Toloba et al. 2016; Spengler et al. 2017; Longobardi et al. 2018). We have collected radial velocities from these and other previous works (Binggeli et al. 1985; Hanes et al. 2001; Côté et al. 2003; Brinchmann et al. 2008; Strader et al. 2011, 2012; Pota et al. 2013, 2015; Blom et al. 2014; Norris et al. 2014; Li et al. 2015; Forbes et al. 2017; Ko et al. 2017; Toloba et al. 2018), as well as from the NASA/IPAC Extragalactic Database (NED),[21] the SIMBAD Astronomical Database[22] (Wenger et al. 2000), and the Sloan Digital Sky Survey (SDSS; Abolfathi et al. 2018). In all, we have a total of 31,346 velocity measurements for objects in the NGVS footprint brighter than $g_0 = 21.5$ mag. This database includes foreground stars, GCs, UCDs, galaxies in Virgo, and BGs. In what follows, we make use of this large velocity catalog to eliminate contaminants from our photometric UCD selection as well as to recover UCDs that miss our cuts.

[21] https://ned.ipac.caltech.edu/
[22] http://simbad.u-strasbg.fr/simbad/

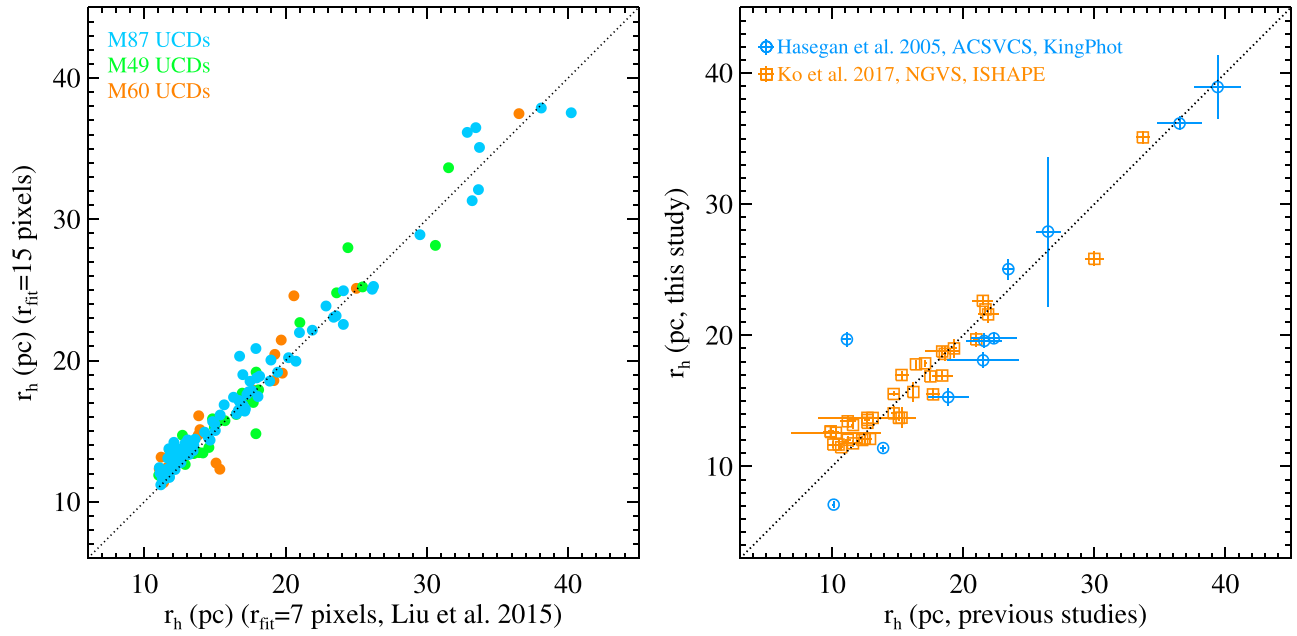

Figure 3. Left panel: comparison of r_h measurements for UCDs based on different fitting radii, $r_{\rm fit}$ (7 vs. 15 pixels), with data taken from Liu et al. (2015a). Right panel: comparison of r_h measured using different data (blue circles, ACSVCS data, Haşegan et al. 2005) or different methods (orange squares, ISHAPE software, Ko et al. 2017).

2.2. Size Measurements

Size is the defining parameter of UCDs.[23] As shown by Liu et al. (2015a), the excellent image quality of the NGVS allows us to measure reliable sizes for compact objects in Virgo (mainly GCs, UCDs, and galactic nuclei) larger than ∼10 pc (see their Section 2.3). We measure half-light radii using the KINGPHOT package (Jordán et al. 2005), focusing on the g and i bands because of the former's depth and the latter's exquisite seeing. Comparisons of the two sets of r_h measurements show that they are consistent with each other (see Figure 3 in Liu et al. 2015a). Jordán et al. (2005) show that KINGPHOT r_h measurements are biased to larger values when $r_h \gtrsim r_{\rm fit}/2$ (where $r_{\rm fit}$ is the fitting radius within which we adopt KINGPHOT), which is ∼50 pc for an $r_{\rm fit} = 7$ pixels (used in Liu et al. 2015a) at the distance of Virgo. This choice of $r_{\rm fit}$ is reasonable because previous works show that most UCDs are smaller than 40 pc (Brodie et al. 2011; Chiboucas et al. 2011; Strader et al. 2011; Penny et al. 2012). However, in the interests of determining whether there are larger UCDs in Virgo, we run KINGPHOT with $r_{\rm fit} = 15$ pixels in this study. Thus, our KINGPHOT measurements would be biased for objects with $r_h \gtrsim 110$ pc.

The left panel of Figure 3 compares our UCD r_h measurements from Liu et al. (2015a) for the two values of $r_{\rm fit}$ above. We note that the larger $r_{\rm fit}$ yields slightly larger sizes when $r_h \lesssim 16$ pc. Otherwise, the two sets of r_h measurements are statistically equivalent, so we therefore adopt the KINGPHOT measurements made with $r_{\rm fit} = 15$ pixels. The right panel of this figure shows a comparison between the r_h measurements from this work and those from previous studies. The blue circles are taken from Haşegan et al. (2005), who measured r_h using KINGPHOT and HST data (ACSVCS; Côté et al. 2004). The orange squares denote the r_h measurements from Ko et al. (2017), who used ISHAPE software and NGVS data. From this figure, we can see that our r_h measurements are consistent with the measurements from previous studies, even though they used different methodologies and/or data sets.

3. UCD Selection

We select UCD candidates within the multidimensional parameter space of magnitude, ellipticity ($e \equiv 1 - b/a$), color, surface brightness, and half-light radius, which we now describe and justify.[24] We begin by adopting simple magnitude cuts of $14.0 < g_0 < 21.5$ mag, where the lower bound corresponds to the saturation limit of our g-band short exposures and the upper bound to the limit of accurate measurements of half-light radii (see Section 2 in Liu et al. 2015a for details). We also apply a simple cut on ellipticity, adhering to the empirical result that most spectroscopically confirmed UCDs in Virgo (i.e., $v_r < 3500\,{\rm km\,s^{-1}}$) have $e < 0.3$ (see, e.g., Zhang et al. 2015).

As we have previously shown (Muñoz et al. 2014; Liu et al. 2015a; Powalka et al. 2016a, 2016b), the combination of u^*giK_s photometry proves to be a highly effective tool for discriminating extragalactic GCs and UCDs from BGs and foreground stars. Unfortunately, Figure 1 shows that we only have K_s-band imaging for the central 4 deg^2 of subcluster A from the NGVS-IR (see Muñoz et al. 2014 for details). Moreover, in the u^* and i bands, only partial coverage is available in the short-exposure category. In an attempt to balance homogeneity and accuracy, we base the color portion of our UCD selection on our u^*, g, i, z, and UKIDSS K-band photometry. The UKIDSS data, although shallower than those from NGVS-IR, are sufficient for our purpose, i.e., to select UCD candidates with $g_0 < 21.5$ mag. We will describe our u^*giK_s- and u^*gizK-based selections and compare their results in the following two subsections.

[23] Unless stated otherwise, we use the term "size" to refer to an object's half-light radius, r_h, exclusively.

[24] It is worth bearing in mind that UCD selection criteria are often driven as much by observational details, such as limiting magnitudes and angular resolution, as by considerations of formation physics.

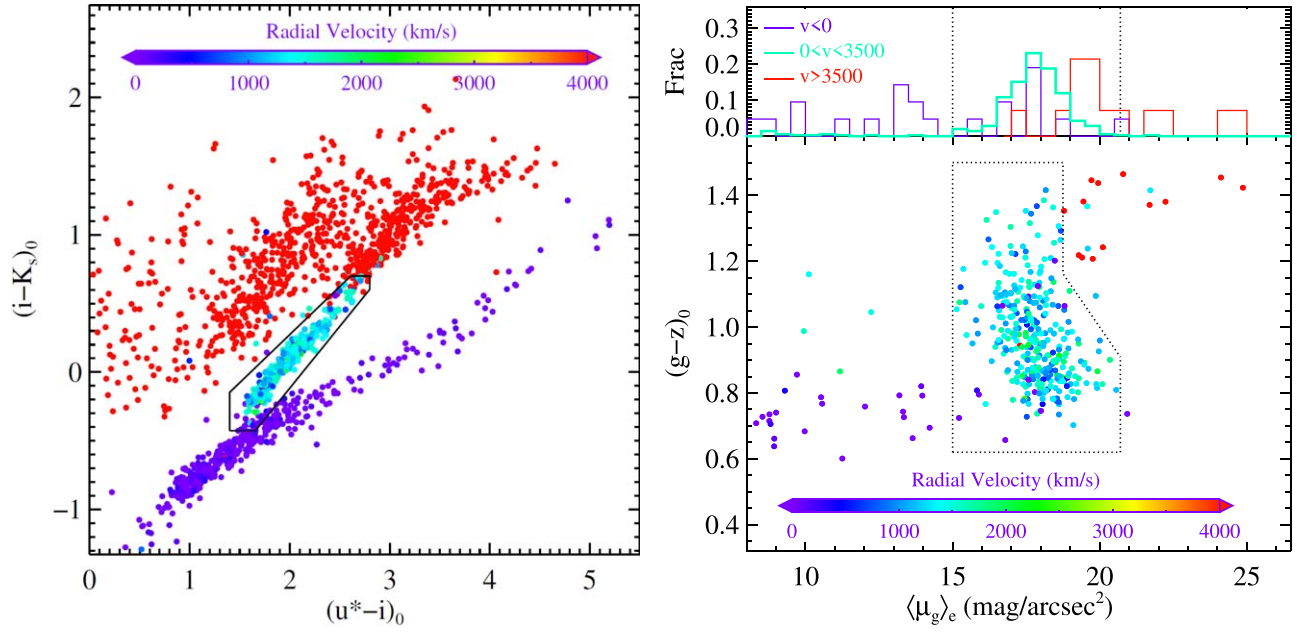

Figure 4. Left panel: the u^*iK_s color–color diagram. The solid polygon represents our GC+UCD selection box in this plane. The points are colored by their associated radial velocity measurements, reflected in the color bar at top. Right panel: the distribution of mean surface brightness, $\langle\mu_g\rangle_e$ (in broad bins of radial velocity; top), and $(g-z)_0$ color as a function of $\langle\mu_g\rangle_e$ for the objects lying within our selection region on the left. The dotted polygon shows the next layer of our selection, based on surface brightness, and the points are colored by their associated radial velocities.

3.1. u*giK$_s$-based Selection

In the left panel of Figure 4, we show the cuts employed as part of our u^*giK_s-based selection. There, we plot in the (u^*-i) versus $(i-K_s)$ plane the ∼2000 objects from our spectroscopic catalog that satisfy our magnitude and ellipticity cuts. The points have been colored by their measured radial velocities and can be divided into three main groups: BGs (red dots; $v \gtrsim 3500\,\mathrm{km\,s^{-1}}$), Virgo members (green and cyan dots; $0 \lesssim v \lesssim 3500\,\mathrm{km\,s^{-1}}$), and foreground stars (blue and purple dots; $v \lesssim 0\,\mathrm{km\,s^{-1}}$).[25] It is clear that Virgo members can be readily distinguished from BGs and foreground stars in the u^*iK_s color–color diagram. To isolate Virgo members, we therefore adopt the following color cuts:

$$\begin{cases} 1.400 \leqslant (u^*-i)_0 \leqslant 2.800; \\ -0.427 \leqslant (i-K_s)_0 \leqslant 0.700; \\ (i-K_s)_0 \leqslant -1.127 + 0.700 \times (u^*-i)_0; \\ (i-K_s)_0 \geqslant -1.917 + 0.900 \times (u^*-i)_0 \end{cases} \quad (1)$$

which are indicated by the irregular polygon in the figure.

The right-hand panel of Figure 4 shows the $(g-z)_0$ color as a function of mean effective surface brightness, $\langle\mu_g\rangle_e$, which is the average surface brightness measured within the half-light radius. The points show those objects that passed our color cuts in the u^*iK_s diagram and, again, are colored according to their radial velocities. It is clear from the distribution that we can use surface brightness to further improve the purity of our Virgo sample by removing BGs and some foreground stars. The dotted polygon shows the exact cuts in surface brightness that we adopt, which are described by the following functions:

$$\begin{cases} 0.620 \leqslant (g-z)_0 \leqslant 1.500; \\ \langle\mu_g\rangle_e \geqslant 15.000\ \mathrm{mag\ arcsec^{-2}}; \\ \langle\mu_g\rangle_e \leqslant 18.750\ \mathrm{mag\ arcsec^{-2}}, \\ \qquad \text{when } 1.163 \leqslant (g-z)_0 \leqslant 1.500; \\ \langle\mu_g\rangle_e \leqslant 27.692 - 7.692 \times (g-z)_0, \\ \qquad \text{when } 0.909 \leqslant (g-z)_0 \leqslant 1.163; \\ \langle\mu_g\rangle_e \leqslant 20.700\ \mathrm{mag\ arcsec^{-2}}, \\ \qquad \text{when } 0.620 \leqslant (g-z)_0 \leqslant 0.909. \end{cases} \quad (2)$$

The combination of the cuts applied to this point leaves us with a broad sample of Virgo members that includes compact elliptical galaxies, galactic nuclei (in low-mass galaxies), UCDs, and GCs. To isolate the UCDs within this sample, we apply one final set of cuts based on our measured half-light radii, which are

$$\begin{cases} 11 < \langle r_h\rangle < 100\ \mathrm{pc}; \\ \dfrac{|r_{h,g} - r_{h,i}|}{\langle r_h\rangle} \leqslant 0.5; \\ \dfrac{r_{h,g,\mathrm{error}}}{r_{h,g}} \leqslant 15\%; \\ \dfrac{r_{h,i,\mathrm{error}}}{r_{h,i}} \leqslant 15\%, \end{cases} \quad (3)$$

where $\langle r_h\rangle$ represents the weighted mean of the half-light radii measured in the g and i bands. These cuts mimic ones often used in previous studies to separate UCDs and GCs (e.g., Brodie et al. 2011; Strader et al. 2011; Penny et al. 2012). Though arbitrary, this is not an unreasonable choice because the typical size of either the MW or extragalactic GCs is ∼3 pc, and most GCs are smaller than ∼10 pc (e.g., van den Bergh et al. 1991;

[25] Note that this very basic redshift classification is not strictly correct; some Virgo members do indeed have negative radial velocities, such as objects belonging to the M86 group (see, e.g., Park et al. 2012; Boselli et al. 2018), and many stars have positive radial velocities (Katz et al. 2019).

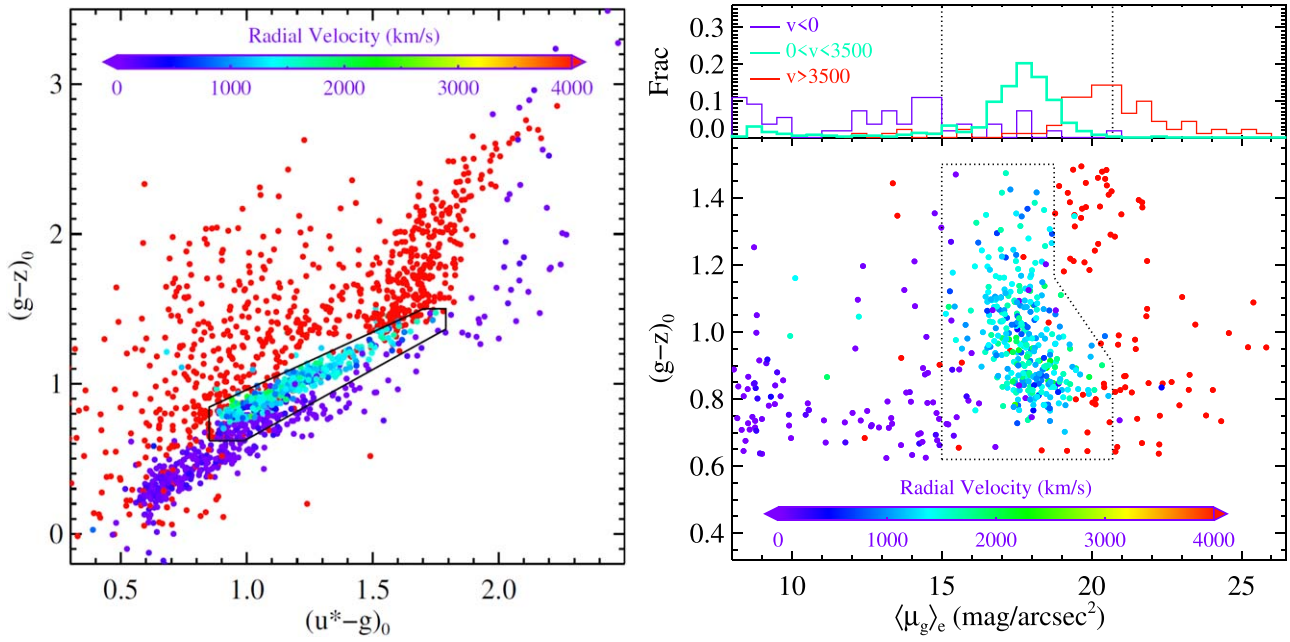

Figure 5. As in Figure 4 but based on the u^*gz color–color diagram instead.

Jordán et al. 2005). Furthermore, Liu et al. (2015a) have shown that r_h measurements based on NGVS imaging are reliable for bright objects ($g_0 < 21.5$ mag) larger than $r_h \sim 10$ pc (see Section 2.3 of their paper). The lower limit on $\langle r_h \rangle$ used in this study roughly matches the limiting resolution of NGVS imaging.

3.2. u*giz- *and* u*gizK-*based Selection*

Given the lack of deep K_s-band imaging over most of the NGVS footprint, we have developed an alternative strategy for selecting UCDs based on the u^*, g, i, z and (where available) K bands. As seen in Figure 1, NGVS imaging is not fully complete in the u^* and i bands for the short exposures. As argued in Muñoz et al. (2014), the u^* band is essential when selecting UCDs due to its sensitivity to young/hot stellar populations, which allows for the removal of background star-forming galaxies. The left panel of Figure 5 shows the u^*gz color–color diagram for the same spectroscopic sample (following the same color-coding) as in Figure 4. In this case, we can see that the spaces occupied by BGs, Virgo members, and foreground stars more heavily overlap with each other. Nevertheless, the Virgo members still form a relatively tight sequence in this plane, such that we can select a sample of these objects with high completeness, albeit with more contamination. We adopt a color selection (represented by the polygon) within this diagram of the form:

$$\begin{cases} 0.850 \leqslant (u^* - g)_0 \leqslant 1.790; \\ 0.620 \leqslant (g - z)_0 \leqslant 1.500; \\ (g - z)_0 \leqslant 0.190 + 0.770 \times (u^* - g)_0; \\ (g - z)_0 \geqslant -0.300 + 0.930 \times (u^* - g)_0. \end{cases} \quad (4)$$

The objects that satisfy these cuts are plotted in the color versus surface brightness plane in the right-hand panel of Figure 5. Although many contaminants pass our color–color cuts, it is possible to eliminate most of these following the same cuts on surface brightness that we applied to our u^*giK_s sample

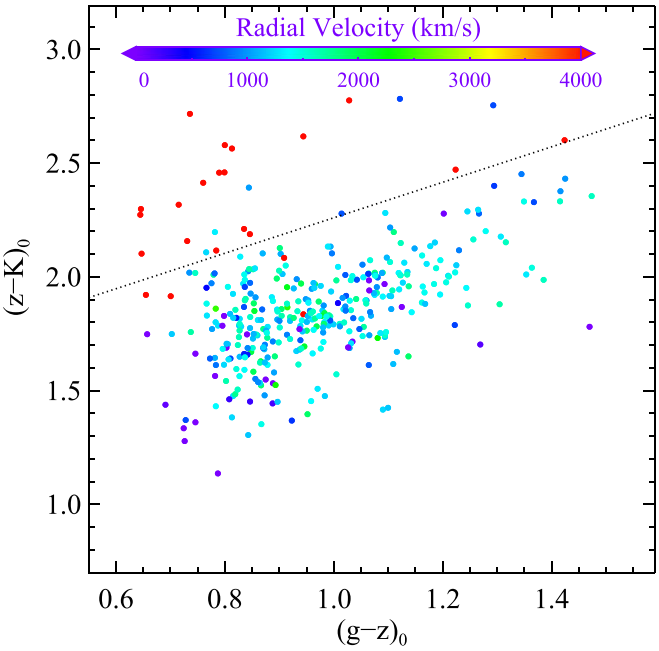

Figure 6. gzK color–color diagram for u^*gz-selected UCD candidates. Different colors indicate different radial velocities as given by the color bar. The black dotted line is used to separate BGs and UCD candidates.

(Equation (2); dotted polygon in this panel). These cuts are not as effective as before, however, and leave behind a number of BGs (red dots). Fortunately, we can remove most of these residual contaminants wherever we have K-band data. Figure 6 shows the gzK color–color diagram for those objects from our spectroscopic catalog that satisfy our u^*gz and surface brightness cuts. For a given $(g - z)_0$ color, BGs tend to be redder in $(z - K)_0$ than Virgo members, and we use the following relationship to isolate the latter:

$$(z - K)_0 \leqslant 1.480 + 0.780 \times (g - z)_0. \quad (5)$$

Table 1
Application of Our Photometric UCD Selection Methods (u^*giK_s, u^*giz, and u^*gizK) to a Spectroscopic Training Set

	u^*giK_s				u^*giz				u^*gizK			
Velocity	$v < 0$	$0 < v < 3500$		$v > 3500$	$v < 0$	$0 < v < 3500$		$v > 3500$	$v < 0$	$0 < v < 3500$		$v > 3500$
Obj. type	Stars	UCDs	dE, Ns	BGs	Stars	UCDs	dE, Ns	BGs	Stars	UCDs	dE, Ns	BGs
$g_0 < 21.5$ & $e < 0.3$	183	71	17	841	183	71	17	841	183	71	17	841
Color–color Diagram	21	71	9	14	55	69	10	91	55	69	10	91
$\langle\mu_g\rangle_e$	8	69	6	1	10	68	7	17	10	68	7	17
$\langle r_h\rangle$	2	67	4	0	2	66	5	14	2	66	5	14
gzK	…	…	…	…	…	…	…	…	2[a]	66[b]	5[c]	1

Notes.
[a] These two "stars" lie in the NGVS-1+1 field, where many Virgo members have negative radial velocities. We consider these two objects as UCDs, in which case all three of our selection methods successfully cull the stars from our training set.
[b] Two of these objects are included in our final UCD catalog, while the remaining three have half-light radii of 0.0, 10.1, and 10.8 pc.
[c] These five objects are included in the Virgo Cluster Catalogue (VCC; Binggeli et al. 1985).

After this, we apply the same size cuts as before (Equation (3)) to arrive at our sample of UCD candidates.

3.3. Comparing Our Selection Methods

In this section, we compare the UCD catalogs derived from the two selection methods described above. For this comparison, the best region within the NGVS footprint is the center of subcluster A, where we have u^*, g, i, z, K_s (NGVS-IR), and K (UKIDSS) band fluxes and radial velocities for ∼2000 objects. Among this sample, 71 are spectroscopically confirmed UCDs that were already known from previous work (mainly Strader et al. 2011 and Zhang et al. 2015).

As described in Section 3.1, we divide these objects into three groups according to their radial velocities: BGs ($v > 3500\,\mathrm{km\,s^{-1}}$), Virgo members ($0 < v < 3500\,\mathrm{km\,s^{-1}}$), and foreground stars ($v < 0\,\mathrm{km\,s^{-1}}$). Within the "Virgo" group, we only consider two subclasses of objects: UCDs and galaxies classified in previous or contemporaneous studies as nucleated dwarf elliptical galaxies, which have identifiable point sources at their centers (Binggeli et al. 1985; Sánchez-Janssen et al. 2019; Ferrarese et al. 2020). Diffuse, non-nucleated dwarfs are explicitly excluded in our selection pipeline.

As listed in Table 1, we have 183 stars, 71 UCDs, 17 dE, Ns, and 841 BGs which satisfy our magnitude and ellipticity criteria (i.e., $14.0 < g_0 < 21.5$ mag and $e < 0.3$). Following this, we successively apply our color, surface brightness, and size cuts, with the choice of colors being the only variable. Table 1 presents the number of objects from each group that survive each step of our selection functions.

For the u^*giK_s-based selection, the color and surface brightness cuts are quite effective at eliminating most of the contaminants. In the end, we find 2 stars (∼1%), 67 UCDs (∼94%), 4 dE, Ns (∼24%), and 0 BGs satisfying all of the criteria.[26] For comparison, we find that 2 stars (∼1%), 66 UCDs (∼93%), 5 dE, Ns (∼29%), and 14 BGs (∼2%) pass the cuts in our u^*giz-based selection. Thus, both methods achieve a completeness of >90% with respect to UCD selection. Conversely, the former method is much better than the latter in culling BGs from the sample. With the addition of K-band data, though, we can reduce the number of BGs that pass our u^*giK-based selection from 14 to 1, which compares very favorably with the results of our u^*giK_s-based selection.

As for the other contaminants, we note that all three of our selection methods pass two objects from our training set that are labeled as foreground stars. In fact, these two objects are really UCDs that have negative radial velocities through their association with the M86 subgroup. This shows that the combination of optical and near-infrared photometry removes most foreground and background objects. Where this photometric combination falls short is in rejecting dE, Ns, but we can easily accomplish this through visual inspection because nuclei are surrounded by obvious envelopes.

To summarize, our tests in the central 4 deg^2 of subcluster A show that a u^*gizK-based selection of UCDs can be a reliable alternative to that based on u^*giK_s. Hereafter, we mainly rely on our u^*gizK selection method to detect UCD candidates wherever K-band data are available and u^*giz otherwise.

3.4. Data Inputs for the Full Catalog

Based on the material presented to this point, the selection of UCDs would ideally rely on data in the u^*gzK bands for color and surface brightness cuts, and in the g and i bands for size cuts. However, as shown in Figure 2, we do not possess imaging in the u^*, i, and K bands over the full NGVS footprint. In Table 2, we list the available combinations of photometric data and the corresponding selection method applied in each case. Approximately 90% of bright objects ($g_0 < 21.5$ mag) detected in the NGVS have data in either the u^*gizK or u^*giz bands; all other objects are covered by some subsample of the five available bands.

Table 2 also shows the number (N_{UCDs}) and the fraction (f_{UCDs}) of UCDs selected by each method. Most of our UCD candidates (∼91%) are selected through either the u^*gizK- or u^*giz-based methods, which were discussed in previous sections. It is noteworthy that only ∼37% (286) of these candidates are selected from ∼60% of our catalog that has u^*gizK data. Proportionally, we expect to find ∼145 UCD candidates from ∼30% of the catalog. However, 465 candidates (∼60%) are selected from the ∼30% of the catalog that do not have K-band data. As described above, K-band data are efficient for eliminating BGs. This suggests that the portion of our UCD sample selected via the u^*giz-based method is inflated through contamination by BGs. Note that the other selection methods we have employed contribute just 28 objects

[26] These percentages represent the fraction of objects, within each group, with $g_0 < 21.5$ mag and $e < 0.3$ that survive all of the selection criteria.

Table 2
Summary of Multiband Data Sets over the NGVS Footprint and the Corresponding UCD Selection Methods

Bands (1)	$f_{\rm Objs}$ (2)	Selection Method (3)	$N_{\rm UCDs}$ (4)	$f_{\rm UCDs}$ (5)	$N_{\rm UCDs,class=1}$ (6)	$f_{\rm UCDs,\ class=1}$ (7)
u^*gizK	59.0%	$u^*gzK + \langle\mu_g\rangle_e + \langle r_h\rangle$	286	34.5%	235	38.4%
u^*giz	29.3%	$u^*gz + \langle\mu_g\rangle_e + \langle r_h\rangle$	465	56.2%	363	59.3%
u^*gzK	2.4%	$u^*gzK + \langle\mu_g\rangle_e + r_{h,g}$	4	0.5%	0	0.0%
u^*gz	0.2%	$u^*gz + \langle\mu_g\rangle_e + r_{h,g}$	1	0.1%	0	0.0%
$gizK$	3.8%	$gzK + \langle\mu_g\rangle_e + \langle r_h\rangle$	1	0.1%	0	0.0%
giz	0.1%	$gz + \langle\mu_g\rangle_e + \langle r_h\rangle$	0	0.0%	0	0.0%
gzK	4.3%	$gzK + \langle\mu_g\rangle_e + r_{h,g}$	9	1.1%	0	0.0%
gz	0.9%	$gz + \langle\mu_g\rangle_e + r_{h,g}$	13	1.6%	0	0.0%
gi+spec	⋯	$(v_r < 3500\ \mathrm{km\ s^{-1}}) + \langle r_h\rangle$	49	5.9%	14	2.3%
Total	100%	⋯	828	100%	612	100%

Note. (1) The available filter combinations, (2) the fraction of the parent sample covered by each filter combination, (3) the UCD selection method employed, (4) the number of UCD candidates selected, (5) the fraction of all UCD candidates selected, (6) the number of UCDs that survive visual inspection, and (7) the fraction of all classified UCDs.

to our UCD sample (or ∼3%). In all, we have identified 779 UCD candidates based on photometry alone.

Finally, we note that if only g- and z-band data are available, we select UCD candidates using the following color cut:

$$0.620 \leqslant (g - z)_0 \leqslant 1.500. \quad (6)$$

Also, if i-band half-light radii are not available, we apply the following cuts to the corresponding g-band value:

$$\begin{cases} 11 < r_{h,g} < 100\ \mathrm{pc}; \\ \dfrac{r_{h,g,\mathrm{error}}}{r_{h,g}} \leqslant 15\%. \end{cases} \quad (7)$$

3.5. Spectroscopically Selected Virgo Members

In Figures 5 and 6, we see that a few confirmed Virgo members fall outside our color selection windows. Some of these objects lie close to the window boundaries, however, and therefore could be UCD candidates. The purpose of our color selection criteria is, first and foremost, to reduce or eliminate contamination from BGs. For these few cases, if we know from their radial velocities that they are not background objects, then we do not require color criteria. We assume that the Virgo members are UCDs if they satisfy our size cuts (Equation (3) or (7) if i-band data are not available). This assumption is reasonable as most objects in the literature in this size range are UCDs. There are ∼8000 Virgo objects with $v < 3500\ \mathrm{km\ s^{-1}}$ and do not satisfy our color or/and surface brightness cuts. Among these objects, we find an additional 49 UCD candidates through this "perturbation" method and henceforth refer to them as "spectroscopically selected UCD."

In Table 1, we recover 66 of the 71 known UCDs using either our u^*giz- or u^*gizK-based methods (the remaining 5 do not meet all of our selection criteria). In reality, two of these five "missing" UCDs are included in the spectroscopically selected UCD sample. The three remaining UCDs have $\langle r_h\rangle = 0.0$ (due to the bad image quality in this region), 10.1, and 10.8 pc individually: i.e., two of the three are slightly smaller than our size criterion.

3.6. Visual Inspection

As explained above, we have objectively selected 828 UCD candidates: 779 and 49 based on photometric and spectroscopic information, respectively. As a final hedge against contamination, we execute one last step—visual inspection of the NGVS images, whereby we classify each candidate as either a (1) = `probable UCD`; (2) = `dwarf nucleus`; (3) = `background galaxy`; (4) = `blended object`; (5) = `star`; or (6) = `star-forming region`.

Some contaminants can be difficult to identify from visual inspection alone, and in such cases, we classify objects using additional information. For example, a nucleated dwarf galaxy (`class = 2`) usually contains a nucleus at its photocenter (although some are slightly off centered) and a stellar halo component surrounding it. Some UCDs are also embedded in low-surface-brightness envelopes (e.g., Haşegan et al. 2005), making it difficult to distinguish dE, Ns from UCDs with envelopes. We therefore classify objects as dE, Ns only when they appear in either the VCC (Binggeli et al. 1985) or NGVS galaxy catalogs (Ferrarese et al. 2020). BGs are identified with the help of redshift measurements, and all objects with $v_r > 3500\ \mathrm{km\ s^{-1}}$ are immediately classified as such (`class = 3`). Blended objects (`class = 4`) are relatively easy to identify, although they may not be separable in NGVS images if they are too close. We make use of Gaia DR2 data (Riello et al. 2018) to help further separate UCDs and stars (`class = 5`), in that stars can have significant proper motions (i.e., 3σ significance) and UCDs can be resolved in Gaia imaging (see Voggel et al. 2020). Figure 7 shows the BP/RP flux-excess factor, which is defined as the flux ratio $(I_{\rm BP} + I_{\rm RP})/I_G$, as a function of Gaia G-band magnitude. Briefly, the fluxes in the BP and RP bands ($I_{\rm BP}$ and $I_{\rm RP}$) are measured in a window of $3.5 \times 2.1\ \mathrm{arcsec}^2$ while the flux in G band (I_G) is derived from PSF fitting. For point sources, the flux-excess factor should be $\gtrsim$1 (the BP and RP filters overlap at around 6500 Å and are broader than the G band, especially at the red side; see Evans et al. 2018). As shown in Figure 7, most of Gaia targets have small flux-excess factors while the excess

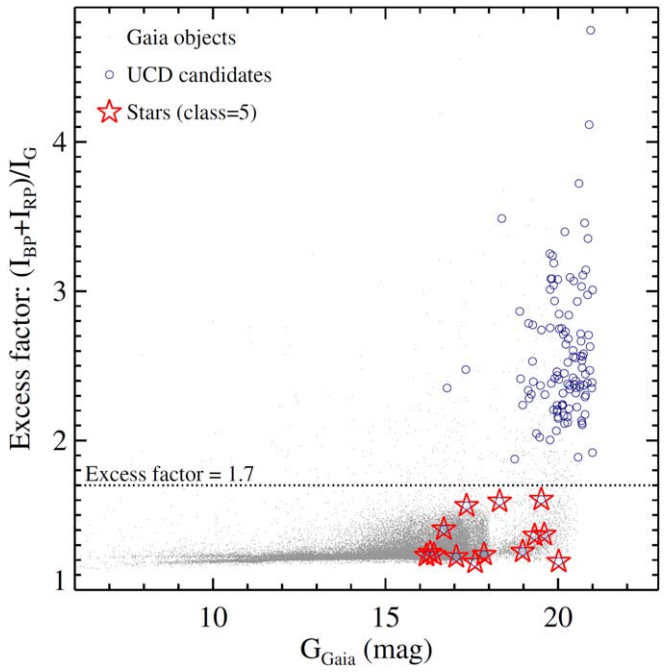

Figure 7. Gaia BP/RP flux-excess factor—$(I_{BP} + I_{RP})/I_G$—as a function of G-band magnitude. Gray dots are Gaia sources in the NGVS footprint. Blue circles are UCD candidates that have a Gaia counterpart. Red stars are objects classified as stars (`class = 5`) in this study. The black dotted line shows an excess factor of 1.7, a division that is found to separate stellar and extended sources.

factor of extended objects can be much larger: e.g., most of our UCD candidates (blue circles) in Figure 7 have excess factors of 2–4. We draw a line at an excess factor of 1.7 and classify sources below this level as stars. Finally, the star-forming regions (`class = 6`) are also easy to identify due to their blue colors.

In summary, among our 828 UCD candidates, we find 612 probable UCDs (598 identified on the basis of photometry alone), 41 nucleated dwarf galaxies, 132 BGs, 12 blended objects, 14 stars, and 17 star-forming regions. Representative images for these six types of objects are shown in Figure 8. As can be seen in the final two columns of Table 2, 235 of the photometrically identified UCDs are u^*gizK selected while the remaining 363 are u^*giz selected. The UCD candidates initially selected based on other methods (i.e., u^*gzK, u^*gz, $gizK$, giz, gzK, and gz) are classified as contaminants after visual inspection—one of the reasons that we only test the u^*giz- and u^*gizK-selection methods in Section 3.3.

3.7. Catalog of UCD Candidates

Tables 3 and 4 present observed and derived parameters for all of our UCD candidates. Since visual inspection is inevitably subjective, we list all 828 objectively selected candidates in these tables.[27] We plan to measure radial velocities in future spectroscopic campaigns and assess their Virgo membership directly. Indeed, some of these "contaminants" (such as apparent star-forming regions with UCD-like sizes) are interesting in their own right and will be investigated in future papers.

[27] The UCD catalog can be downloaded from https://gax.sjtu.edu.cn/data/UCDs.html.

3.8. Summary of UCD Selection Function

Given the complexity of our methodology, Figure 9 summarizes our UCD selection function in the form of a flowchart. An inspection of this figure shows that our selection process involves two main channels: one based on photometry (right) and the other on spectroscopy (left), which we now describe.

We begin with the photometric algorithm. There are 346,948 objects in the NGVS that satisfy our magnitude ($14.0 < g_0 < 21.5$ mag) and ellipticity ($e < 0.3$) cuts. All of these objects have g- and z-band data, while u^*-, i- and K-data are more limited. Note that only objects detected in our short exposures lack u^*- and i-band data (see Figure 2) and so are drawn from the bright end of the UCD luminosity function (UCDLF). We then apply successive cuts based on each object's color (or colors), surface brightness (Equation (2)), position in the gzK diagram (Equation (5); if K-band data are available), and half-light radius (Equation (3) if i-band data are available, otherwise Equation (7)). Our color cuts are based on the u^*gz diagram (Equation (4)) for those objects having u^*-band data; otherwise, we consider the $(g - z)$ color alone (Equation (6)).

These selection criteria dramatically reduce our original photometric sample from 346,948 objects to 779 candidate UCDs. With the assistance of Gaia (see Figures 7), 11 of these candidates are reclassified as stars. To further reduce the number of contaminants, we place a cut on radial velocities (when available) and visually inspect the candidates (see Figure 8). Another 51 candidates are removed for having a radial velocity in excess of $v = 3500\,\mathrm{km\,s^{-1}}$ and 119 more are removed following visual inspection. The latter group is comprised of 27 dE, Ns, 81 BGs, and 11 blended objects. Our final photometric UCD sample contains 598 UCD candidates.

We now describe the spectroscopic selection function depicted in Figure 9. As stated earlier, this path is intended to select UCD candidates that fall outside our color and/or surface brightness selection windows. Using this approach, we find 49 more candidates that meet our radius cuts, while visual inspection shows that they comprise 14 probable UCDs, 17 star-forming regions, 14 dE, Ns, 3 stars, and 1 blended object.

Overall, we have identified 612 UCD candidates, the majority of which (598) come from our photometric selection function. This constitutes the largest sample of UCD candidates identified to date. While we would prefer a simple and homogeneous selection, the lack of data in the u^*, i, and K bands over the full NGVS footprint necessitates certain compromises. That said, the great majority ($598/612 \simeq 97.7\%$) of these UCD candidates have been selected based on their u^*giz or u^*gizK colors.

We refer to the full group of candidates as the "`all UCD sample`." Within this group, 235 candidates have been selected on the basis of their u^*gizK data, so we refer to this as the "u^*gizK `UCD sample`." We also have a "`spec-UCD sample`," which contains the 203 candidates that have been spectroscopically confirmed as members of the Virgo cluster. The "`all UCD sample`" has the highest completeness but the largest number of contaminants. Conversely, the "`spec-UCD sample`" has the fewest contaminants but is inevitably biased by the choice of spectroscopic targets. Finally, the "u^*gizK `UCD sample`" strikes the greatest balance between completeness, contamination, and homogeneity (see Table 1).

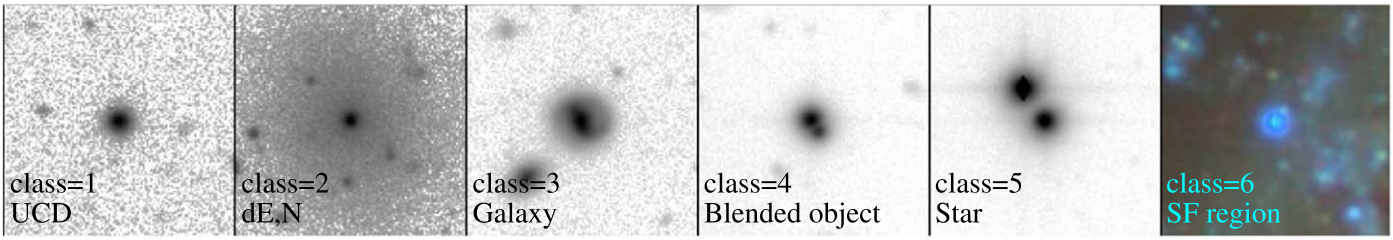

Figure 8. UCD candidates are divided into six classes by visual inspection. From left to right: UCD—class = 1; nucleated dwarf elliptical galaxy (dE, N)—class = 2; background galaxy—class = 3; blended object—class = 4; star—class = 5; star-forming region—class = 6. The image size in each panel is 120 × 120 pixels, where 120 pixels ∼22.″32 ∼1.8 kpc at Virgo distance.

3.9. UCDs from Previous Studies

As nearest rich cluster of galaxies, many previous investigations have studied UCDs in Virgo (e.g., Haşegan et al. 2005; Jones et al. 2006; Evstigneeva et al. 2007b; Strader et al. 2011; Liu et al. 2015a; Zhang et al. 2015; Ko et al. 2017). Our sample contains 186 UCDs that have already been reported, while 29 systems from previous work are excluded. We list the properties of each member of the latter group in Table 5, including name, R.A., decl., ellipticity, magnitude, half-light radius, radial velocity, the sources of velocity measurements, and the primary reason why it is not included in our sample. Among these 29 UCDs, 6 are fainter than $g_0 = 21.5$ mag, 3 have high ellipticity ($e > 0.3$), 12 do not satisfy the radius criteria, 4 are located just outside the selection window in $(g - z)_0$ versus μ_g diagram, 2 are classified as BGs by *gzK* diagram, and 2 escaped detection in the NGVS images because they are projected close to saturated stars. We also note that 9 of these 29 UCDs lack radial velocity measurements.

4. Results

To understand the nature and origin of UCDs—and the extent to which they differ from other compact stellar systems—it is important to first understand how their properties compare to those of GCs and nuclei, where evolutionary links to UCDs may exist. To this end, we now describe various samples of each class of compact stellar system in Virgo available to us.

Globular Clusters:

1. `ACSVCS GCs`: The sample of GCs from the HST ACS Virgo Cluster Survey. The objects with $p_{gc} > 0.95$ are included in this sample, where p_{gc} represents the probability that an object is a GC (Peng et al. 2006b; Jordán et al. 2009).
2. `Bright GCs`: A magnitude-limited ($g_0 < 21.5$ mag) sample of NGVS objects that satisfy our UCD selection criteria but have $\langle r_h \rangle < 11$ pc. This sample includes GC candidates without velocity measurements and GCs with $v_r < 3500\,\mathrm{km\,s^{-1}}$. BGs with $v_r > 3500\,\mathrm{km\,s^{-1}}$ are removed from the sample.
3. `Spec GCs`: The subset of `bright GCs` with radial velocities $v_r < 3500\,\mathrm{km\,s^{-1}}$.

Ultracompact Dwarfs:

1. `All UCDs`: Our full sample of 612 UCD candidates, which satisfy all of our selection criteria and pass our visual inspection. Among this sample, 203 (∼1/3) have $v_r < 3500\,\mathrm{km\,s^{-1}}$; all others lack radial velocity information.
2. u^*gizK `UCDs`: The subset of 235 UCDs selected from u^*gizK data, a fraction of which have velocity measurements.
3. `Spec UCDs`: The subset of 203 UCDs with $v_r < 3500\,\mathrm{km\,s^{-1}}$.

Stellar Nuclei:

1. `All nuclei`: The entire sample of 551 nuclei from the NGVS galaxy catalog (Sánchez-Janssen et al. 2019; Ferrarese et al. 2020).
2. `Bright nuclei`: The subset of 339 bright ($g_0 < 21.5$ mag) nuclei from the NGVS galaxy catalog.
3. u^*gizK `nuclei`: The sample of 41 nuclei that satisfy our UCD selection criteria and are classified as dE, Ns by visual inspection (i.e., `class = 2`).

In the analysis that follows, we mainly focus on the `bright GCs`, u^*gizK `UCDs`, and `bright nuclei` samples. This means that, for the first time, we are using homogeneous samples of GCs, UCDs, and nuclei selected from the same data set using consistent selection criteria. We also use the `ACSVCS GCs`, `all UCDs`, and `all nuclei` samples when we require higher completeness, while the `spec GCs` and `spec UCDs` samples are drawn on when cleaner samples are required.

A complementary approach is to study individual UCDs with special properties that can shed light on their origins. For example, Seth et al. (2014) found an SMBH in M60-UCD1, which comprises 15% of the system's total mass. This single piece of evidence strongly suggests that the progenitor of M60-UCD1 was a nucleated dwarf galaxy.

In this section, we will summarize the basic statistical properties of our UCD samples, compare to those of GCs and nuclei, and examine interesting subsamples of UCDs found in the NGVS (e.g., Liu et al. 2015b).

4.1. Spatial Distribution

The upper two panels of Figure 10 show number density maps for our `all UCDs` sample in Virgo. Durrell et al. (2014) found that the spatial distribution of Virgo GCs is similar to that of its X-ray-emitting gas, so we compare the distribution of UCDs (color-coded number density map) and X-ray gas (contours) in panel (a) of Figure 10. Consistent with Durrell et al. (2014), we find that the densest concentrations of UCDs (i.e., the brightest regions in the map) are located in the regions that have the greatest amount of X-ray gas. This finding is also consistent with the observed correlation between number of UCDs and the X-ray gas mass of their host (N_{UCD} versus M_{gas}; see Figure 17 in Liu et al. 2015a).

The number density map shown in panel (b) is the same as in panel (a), but overlaid with known substructures in the cluster (i.e., the colored circles). The locations and radii of the substructures are taken from Boselli et al. (2014). Most of the UCDs are concentrated in subcluster A (green), subcluster B

Table 3
Photometric Properties of UCD Candidates

ID	Name	NGVSID	t_{obs}	α_{J2000} (deg)	δ_{J2000} (deg)	$E(B-V)$ (mag)	g_0 (mag)	K (mag)	$(u^*-g)_0$ (mag)	$(g-i)_0$ (mag)	$(g-z)_0$ (mag)	Δ_{env} (mag)	UCD
(1)	(2)	(3)	(4)	(5)	(6)	(7)	(8)	(9)	(10)	(11)	(12)	(13)	(14)
1	NGVS-UCD1	NGVS-J120652.65+113246.5	l	181.7193703	11.5462618	0.028	19.212 ± 0.002	⋯	0.554 ± 0.004	−0.034 ± 0.004	−0.034 ± 0.006	0.018	0
2	NGVS-UCD2	NGVS-J120717.93+113846.7	l	181.8247260	11.6463089	0.032	21.074 ± 0.003	⋯	0.984 ± 0.011	0.650 ± 0.007	0.822 ± 0.010	0.105	1
3	NGVS-UCD3	NGVS-J120734.18+113626.0	l	181.8924309	11.6072260	0.028	21.492 ± 0.004	⋯	1.062 ± 0.011	0.600 ± 0.007	0.709 ± 0.012	0.032	1
4	NGVS-UCD4	NGVS-J120755.71+113921.2	l	181.9821228	11.6558897	0.030	21.057 ± 0.003	⋯	0.892 ± 0.008	0.633 ± 0.006	0.725 ± 0.010	0.079	1
5	NGVS-UCD5	NGVS-J120757.12+121954.2	l	181.9879964	12.3317198	0.027	21.444 ± 0.004	⋯	1.089 ± 0.011	0.648 ± 0.007	0.723 ± 0.012	0.005	0
6	NGVS-UCD6	NGVS-J120811.52+131327.6	l	182.0480094	13.2243239	0.030	21.408 ± 0.004	⋯	0.910 ± 0.012	0.525 ± 0.009	0.673 ± 0.019	0.015	1
7	NGVS-UCD7	NGVS-J120827.25+132407.4	l	182.1135389	13.4020547	0.032	21.373 ± 0.004	⋯	0.920 ± 0.010	0.656 ± 0.007	0.724 ± 0.013	0.009	1
8	NGVS-UCD8	NGVS-J120846.23+121935.8	l	182.1926310	12.3266129	0.026	21.338 ± 0.003	⋯	0.970 ± 0.010	0.770 ± 0.007	0.852 ± 0.012	0.032	1
9	NGVS-UCD9	NGVS-J120855.90+121833.2	l	182.2329343	12.3092174	0.027	21.415 ± 0.004	⋯	1.032 ± 0.011	0.796 ± 0.007	0.892 ± 0.011	0.060	1
10	NGVS-UCD10	NGVS-J120925.56+132007.7	l	182.3565013	13.3354611	0.034	19.007 ± 0.001	⋯	0.877 ± 0.003	0.588 ± 0.002	0.711 ± 0.003	0.197	0

Note. (1) Identification number; (2) UCD name; (3) object name in NGVS catalog; (4) exposure time: l = selected using long-exposure data, s = selected using short-exposure data; (5) R.A. in decimal degrees; (6) decl. in decimal degrees; (7) Galactic extinction according to Schlegel et al. (1998); and (8) Galactic-extinction-corrected, aperture-corrected g-band magnitude found within a 16 pixel (∼3″) diameter aperture. For details, see Liu et al. (2015a); (9) UKIDSS (Lawrence et al. 2007) K-band magnitude within a 3″ diameter aperture; (10–12) color index measured in an 8 pixel (∼1.″5) diameter aperture, Galactic extinction corrected; (13) envelope parameter: $\Delta_{env} \equiv g_{16} - g_{32}$, where g_{16} and g_{32} are magnitudes in 16 and 32 pixel diameter apertures; and (14) object flag: 0 = `contaminant`, 1 = `confirmed or possible UCD`.

(This table is available in its entirety in machine-readable form.)

Table 4
Structural Properties and Other Information for UCD Candidates

Name	M_B (mag)	M_V (mag)	$\langle r_h \rangle$ (pc)	$\log(M_*/M_{\odot dot})$	v_r (km s^{-1})	v_{source}	Class	Envelope	Method	Other Name
(1)	(2)	(3)	(4)	(5)	(6)	(7)	(8)	(9)	(10)	(11)
NGVS-UCD1	−11.62	−11.38	14.03 ± 0.39	6.5	−38	SDSS	5	0	$(v_r < 3500 \mathrm{km\ s^{-1}}) + \langle r_h \rangle$	⋯
NGVS-UCD2	−9.68	−9.21	29.86 ± 0.76	6.3	⋯	⋯	1	0	$u^*gz + \langle \mu_g \rangle_e + \langle r_h \rangle$	⋯
NGVS-UCD3	−9.27	−8.76	15.34 ± 0.38	6.1	⋯	⋯	1	0	$u^*gz + \langle \mu_g \rangle_e + \langle r_h \rangle$	⋯
NGVS-UCD4	−9.70	−9.27	29.48 ± 0.54	6.2	⋯	⋯	1	0	$u^*gz + \langle \mu_g \rangle_e + \langle r_h \rangle$	⋯
NGVS-UCD5	−9.33	−8.80	22.44 ± 0.28	6.1	⋯	⋯	3	0	$u^*gz + \langle \mu_g \rangle_e + \langle r_h \rangle$	⋯
NGVS-UCD6	−9.36	−8.93	24.29 ± 1.07	6.0	⋯	⋯	1	0	$u^*gz + \langle \mu_g \rangle_e + \langle r_h \rangle$	⋯
NGVS-UCD7	−9.40	−8.97	24.51 ± 0.37	6.1	⋯	⋯	1	0	$u^*gz + \langle \mu_g \rangle_e + \langle r_h \rangle$	⋯
NGVS-UCD8	−9.41	−8.95	23.33 ± 0.37	6.2	⋯	⋯	1	0	$u^*gz + \langle \mu_g \rangle_e + \langle r_h \rangle$	⋯
NGVS-UCD9	−9.30	−8.80	25.00 ± 0.68	6.2	⋯	⋯	1	0	$u^*gz + \langle \mu_g \rangle_e + \langle r_h \rangle$	⋯
NGVS-UCD10	−11.80	−11.39	65.92 ± 0.72	7.0	⋯	⋯	3	0	$u^*gz + \langle \mu_g \rangle_e + \langle r_h \rangle$	⋯

Note. (1) UCD name; (2–3) absolute B- and V-band magnitude, calculated using the transformation equation $B = u^* - 0.8116(u^* - g) + 0.1313$, $V = g - 0.2906(u^* - g) + 0.0885$ (http://www.sdss3.org/dr10/algorithms/sdssUBVRITransform.php#Lupton2005) and a distance modulus of 31.1 mag (Mei et al. 2007; Blakeslee et al. 2009); (4) weighted mean half-light radius in the g and i bands, $\langle r_h \rangle = r_{h,g}$ if an i-band measurement is not available; (5) stellar mass; (6) heliocentric radial velocity (or weighted mean value if multiple measurements are available); (7) the source of our adopted v_r measurement, SDSS: Abolfathi et al. (2018); NED: NASA/IPAC Extragalactic Database; SIMBAD: SIMBAD Astronomical Database (Wenger et al. 2000); VCC: Binggeli et al. (1985); NTT17: NTT 2017 program; AAT 12: AAT 2012 program; MMT 09: MMT 2009 program; Toloba2018: Toloba et al. (2018); Ko2017: Ko et al. (2017); MMT 14: MMT 2014 program; Keck: Keck program; C03: Côté et al. (2003); IMACS 16: Magellan/IMACS 2016 program; S11: Strader et al. (2011); (8) class parameter: 1 = `probable UCD`, 2 = `dwarf nucleus`, 3 = `background galaxy`, 4 = `blended object`, 5 = `star`, 6 = `star-forming region`; (9) envelope: 0 = `lacks obvious envelope`, 1 = `has obvious envelope`; (10) selection method; and (11) alternative names, if available.

(This table is available in its entirety in machine-readable form.)

(blue), and subcluster C (yellow; see also Liu et al. 2015a). There are far fewer UCDs in the other three substructures: the W' (cyan), W (purple), and M clouds (red). This may be due, in part, to the fact that these three substructures are located farther away from us (Mei et al. 2007; Cantiello et al. 2018), making it more difficult to identify UCDs (by size). At the same time, the reduced gas mass (see the contours in panel (a)) in these substructures are also likely to be a factor. This is especially true for the M cloud, which shows no significant amount of X-ray gas. Based on the N_{UCD}–M_{gas} scaling relation (Liu et al. 2015a) then, the absence of UCDs in this region would not be surprising. In addition, the edges of the NGVS footprint cut through the M and W clouds. This may be another reason why we do not detect many UCDs in these regions.

The lower two panels of Figure 10 show number density maps for our u^*gizK `UCDs` sample. As noted above, and as can be seen in the plots, this sample is noticeably cleaner. We also point out that the number densities from the `all UCDs` sample are higher in the regions without UKIDSS K-band data (above the white dashed lines in panels (a) and (b)), indicating elevated contamination in this region. The u^*gizK `UCDs` are mainly concentrated around a handful of luminous galaxies: e.g., M87, M49, M60, M59, M86, and M89 (black crosses). The galaxies with low densities of UCDs cannot be seen in this map as we smooth the distribution using a large kernel ($\sim 12' \sim 60$ kpc).

Table 8 of Liu et al. (2015a) presents estimates of the number density of contaminants in the NGVS based on four control fields. The mean density for our u^*giz-selection method is 2.25 deg^{-2}. As demonstrated in Section 3.3, our u^*gizK-selection method should be much cleaner by comparison. Indeed, Liu et al. (2015a) estimated the contaminant number density using their u^*giK_{VISTA} selection method to be just 0.9 deg^{-2} (the last row of their Table 8). The contours in panel (d) represent number densities of $\Sigma_{UCD} = 5$, 8, 15, 30 and 60 deg^{-2}. We note that there are a few regions with $\Sigma_{UCD} > 5$ deg^{-2} that fall outside of any known substructures. They may be intracluster UCDs or UCDs associated with low- or intermediate-mass galaxies (e.g., Fahrion et al. 2019). We intend to focus on these regions in future papers.

4.2. Luminosity and Stellar Mass Distribution

Our homogeneous sample provides us with an opportunity to carry out a study of the UCDLF. The left panel of Figure 11 shows histograms of z-band magnitudes for a variety of UCD samples, which are identified in the upper-left corner. The distribution for the `all UCDs` sample (blue, short-dashed histogram) has a higher peak value than all other UCD samples, which we suspect is due to contamination (especially at the faint end). Note that the truncation at $z_0 \sim 21.0$ mag is the result of our magnitude cut at $g_0 = 21.5$ mag and is therefore artificial.

For the other, smaller samples of UCDS, we find a peak at roughly $z_0 \sim 19.75$ mag. Note that the `spec UCDs` sample (orange dotted line) may be biased because brighter UCDs are more amenable to spectroscopic follow-up. The u^*gizK `UCDs` sample (green solid line) has higher completeness than the `spec UCDs` sample but is limited by the shallow UKIDSS K-band imaging, which may cause us to miss some objects at the faint end. The UCD sample from Liu et al. (2015a; black long-dashed line) is the best available based strictly on the u^*giK_s selection method, where the K_s-band data reach to ∼24 mag. For comparison, we also show in Figure 11 the GCLF from the ACSVCS (cyan line), which exhibits the well-known turnover for this population (e.g., Jordán et al. 2007; Villegas et al. 2010). Despite the fact that three of our UCDLFs also exhibit turnovers, we cannot ensure that these features are authentic. It is quite probable that, depending on where we place our (subjective) size cut (set at $r_h = 11$ pc), the prominence and location of this peak would change.

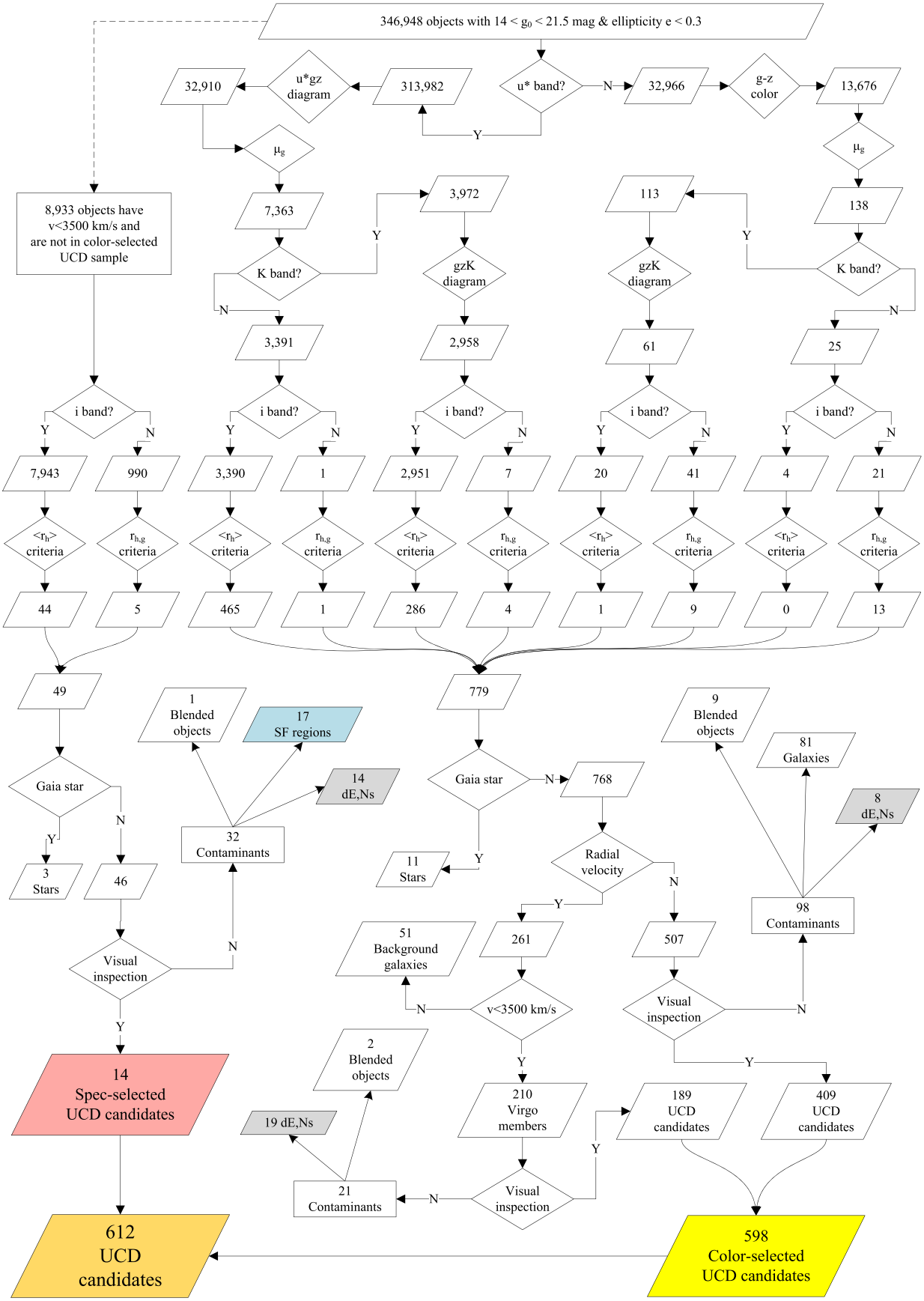

Figure 9. The "Pachinko Machine" plot illustrating the UCD selection methods used in this study. Our UCD selection is based on the combination of magnitude ($14.0 < g_0 < 21.5$ mag), ellipticity ($e \equiv (1 - b/a) < 0.3$), color–color diagram, surface brightness and half-light radius cuts, and visual inspection. In total, a sample of 612 UCDs were identified in NGVS imaging.

Table 5
The Properties of UCDs That Are in Previous Studies but Not Included in This Study

Name	α_{J2000} (deg)	δ_{J2000} (deg)	e	g_0 (mag))	$\langle r_h \rangle$ (pc))	v_r (km s^{-1})	v_{source}	Note
(1)	(2)	(3)	(4)	(5)	(6)	(7)	(8)	(9)
S1508	187.6308727	12.4235661	0.07	22.018	⋯	2419	S11	$g_0 > 21.5$ mag
S825	187.7126346	12.3554004	0.16	21.613	⋯	1142	S11	$g_0 > 21.5$ mag
S723	187.7239811	12.3393933	0.07	21.737	⋯	1398	NED, S11	$g_0 > 21.5$ mag
H44905	187.7378222	12.3944049	0.20	21.921	⋯	1564	NED, S11	$g_0 > 21.5$ mag
H30401	187.8279366	12.2624564	0.18	21.593	⋯	1323	NED, S11	$g_0 > 21.5$ mag
T15886	188.1520299	12.3491986	0.23	22.974	⋯	1349	NED, S11	$g_0 > 21.5$ mag
S991	187.6937514	12.3382605	0.34	20.701	16.67	1004	S11	$e > 0.3$
S672	187.7280306	12.3606434	0.31	20.739	15.50	735	S11	$e > 0.3$
NGVS-J124002.08 +105517.2	190.0086686	10.9214418	0.50	21.338	3.48	⋯	⋯	$e > 0.3$
NGVS-J122926.23 +081658.8	187.3593098	8.2829991	0.05	21.373	9.06	465	MMT 14	$\langle r_h \rangle < 11$ pc
NGVS-J123009.17 +074127.5	187.5381980	7.6909633	0.08	19.449	10.76	⋯	⋯	$\langle r_h \rangle < 11$ pc
NGVS-J123015.56 +083445.0	187.5648407	8.5791729	0.07	20.822	10.33	−129	MMT 14	$\langle r_h \rangle < 11$ pc
H20718	187.5818069	12.1568298	0.03	20.989	10.76	876	MMT 09,S11	$\langle r_h \rangle < 11$ pc
M87UCD-31	187.7305441	12.4110907	0.02	20.860	10.09	1301	MMT 09	$\langle r_h \rangle < 11$ pc
M87UCD-14	187.7681413	13.1784860	0.12	20.200	10.83	1345	MMT 09, AAT 12	$\langle r_h \rangle < 11$ pc
NGVS-J122849.25 +075919.4	187.2051905	7.9887156	0.03	21.179	13.37	⋯	⋯	$\lvert r_{h,g} - r_{h,i} \rvert > (r_{h,g} + r_{h,i})/2$
NGVS-J123004.35 +073932.2	187.5181421	7.6589449	0.09	21.437	11.19	1043	MMT 14	$\lvert r_{h,g} - r_{h,i} \rvert > (r_{h,g} + r_{h,i})/2$
S8005	187.6925322	12.4064233	0.02	20.444	27.91	1883	S11	$\lvert r_{h,g} - r_{h,i} \rvert > (r_{h,g} + r_{h,i})/2$
S9053	187.7013369	12.4946708	0.16	21.313	30.25	829	S11,IMACS 16	$\lvert r_{h,g} - r_{h,i} \rvert > (r_{h,g} + r_{h,i})/2$
S686	187.7242079	12.4718872	0.05	20.499	16.31	817	S11	$\lvert r_{h,g} - r_{h,i} \rvert > (r_{h,g} + r_{h,i})/2$
S6003	187.7922587	12.2744282	0.08	21.277	14.19	1818	S11	$\lvert r_{h,g} - r_{h,i} \rvert > (r_{h,g} + r_{h,i})/2$
NGVS-J122806.14 +065909.0	187.0255686	6.9858243	0.19	20.200	27.66	⋯	⋯	$(g-z)_0$ versus μ_g diagram
NGVS-J123949.21 +110135.3	189.9550398	11.0264758	0.03	21.080	12.73	⋯	⋯	$(g-z)_0$ versus μ_g diagram
NGVS-J124216.65 +114428.6	190.5693756	11.7412681	0.06	21.273	12.44	⋯	⋯	$(g-z)_0$ versus μ_g diagram
NGVS-J124244.72 +111240.5	190.6863239	11.2112384	0.12	20.491	32.90	⋯	⋯	$(g-z)_0$ versus μ_g diagram
NGVS-J122708.94 +074228.3	186.7872607	7.7078639	0.08	19.340	47.81	⋯	⋯	$(g-z)_0$ versus $(z-K_{UKIDSS})_0$ diagram
NGVS-J122828.60 +070228.2	187.1191854	7.0411563	0.11	20.646	28.26	⋯	⋯	$(g-z)_0$ versus $(z-K_{UKIDSS})_0$ diagram
S887	187.7038900	12.3654400	⋯	21.190	⋯	1811	S11	Fail to detect
H30772	187.7419100	12.2672800	⋯	20.750	⋯	1225	NED, S11	Fail to detect

Note. (1) UCD name, (2) R.A., (3) decl., (4) ellipticity, (5) g-band magnitude, (6) half-light radius, (7) radial velocity, (8) the source of velocity measurement, and (9) the reason why this UCD is not included in this study.

The right panel of Figure 11 shows the distributions of stellar mass for UCDs and nuclei. Stellar masses have been determined using the relationships between stellar mass-to-light ratios and colors from Bell et al. (2003). We calculate four sets of stellar masses, based on the relations for $(u-g)$, $(u-i)$, $(u-z)$ and $(g-z)$ colors (see their Table 7), and use the mean value for each object in the figure. Other than the `all UCDs` sample, there appears to be a peak in the UCD stellar mass function at $M_* \sim 10^{6.6}\,M_\odot$, roughly equivalent to that seen in the UCDLF. Again though, because of our selection criteria, we cannot be sure whether this is a genuine characteristic of the UCD population.

The magenta lines in both panels of Figure 11 show the luminosity and mass functions for the `all nuclei` sample that consists of 551 dE, N nuclei. The nuclei LF shows a clear turnover around $z_0 \sim 20.5$ mag and $M_* \sim 10^{6.2}\,M_\odot$, and covers a larger stellar mass range ($10^{5.0} \lesssim M_* \lesssim 10^{8.5}\,M_\odot$) than UCDs. Sánchez-Janssen et al. (2019) studied the mass function of nuclei in the Virgo core region and found a peak at $M_* \sim 10^{6.08}\,M_\odot$, which is consistent with the result in this study.

4.3. Color Distribution

It is well established that bimodal color distributions are a common feature of GC systems in massive elliptical galaxies (e.g., Gebhardt & Kissler-Patig 1999; Kundu & Whitmore 2001; Peng et al. 2006b). Interestingly, a bimodal color distribution has also been observed for the UCDs surrounding

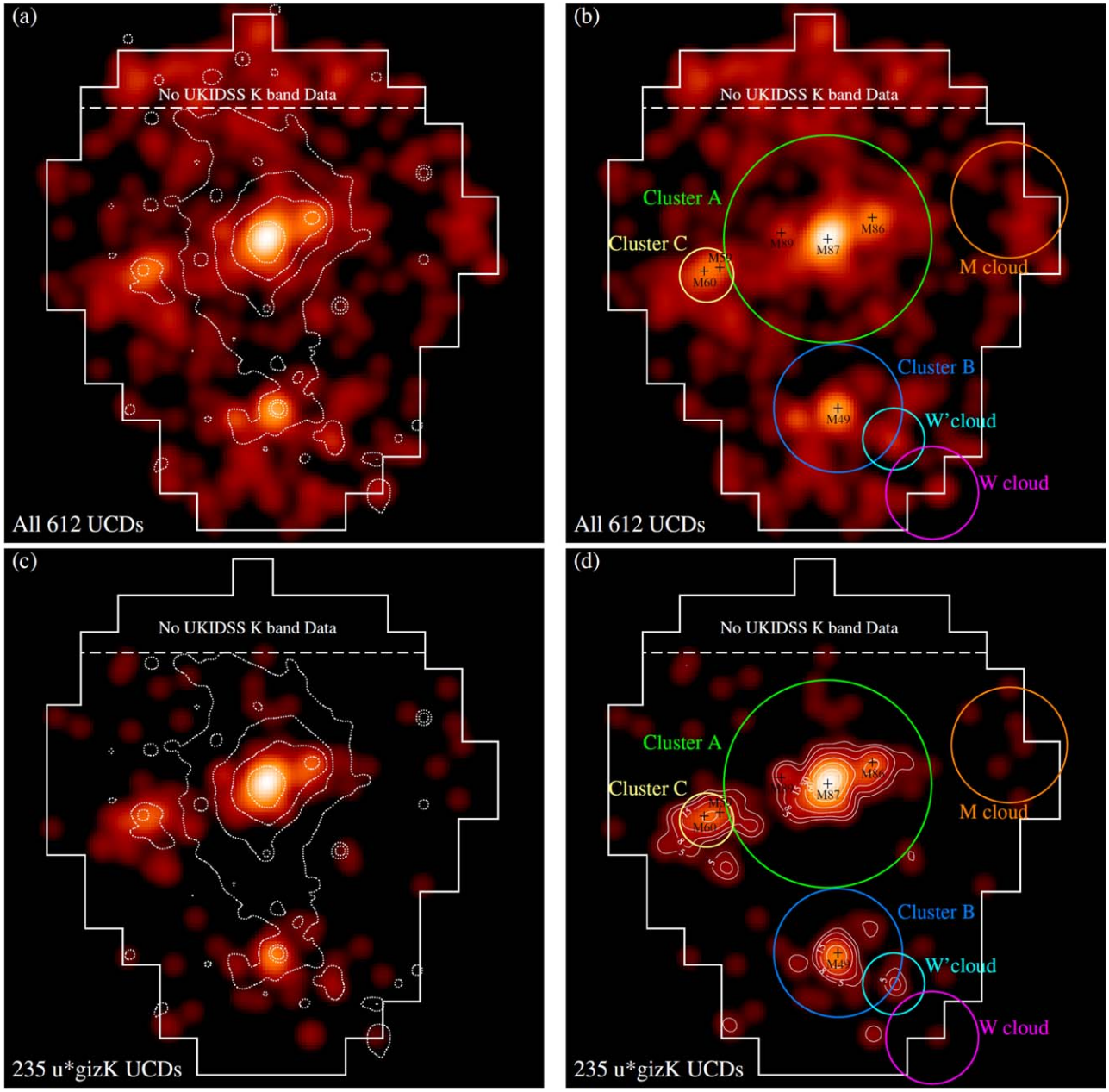

Figure 10. The number density map of 612 `all UCDs` (upper panels) and 235 u^*gizK `UCDs` (lower panels) identified in the NGVS. The maps have been smoothed with a Gaussian kernel with fixed FWHM $\approx 12'$. The white solid polygon in each panel denotes the NGVS survey region. We have no UKIDSS K-band data above the white dashed line in each panel. The contours in the left panels show the distribution of X-rays from the ROSAT all sky survey in the 0.4–2.4 keV energy range (Böhringer et al. 1994). In the right panels, we show the locations of a few bright galaxies (black crosses) and known galaxy substructures (color circles). The contours in panel (d) show the number density contours of $\Sigma_{\rm UCD} = 5$, 8, 15, 30 and 60 deg^{-2}.

M87 (Liu et al. 2015a), making it the only galaxy in the Virgo cluster that shows significant UCD color bimodality.[28] With our new UCD sample, we can examine for the first time the color distribution for UCDs distributed over the entire Virgo cluster.

Figure 12 shows the color distribution for the `ACSVCS GCs` (the first row, magenta histogram), `bright GCs` (the second row, cyan histograms), u^*gizK `UCDs` (the third row, green histograms), and `bright nuclei` (the fourth row, purple histogram). All objects are brighter than $g_0 = 21.5$ mag. Because we have only g and z data for the `ACSVCS GCs`, the first row shows only a $(g - z)_0$ distribution. By contrast, a total of six color indices—$(u^* - g)_0$, $(u^* - i)_0$, $(u^* - z)_0$, $(g - i)_0$, $(g - z)_0$ and $(i - z)_0$—are shown (from left to right) in the second, third, and fourth rows. The distributions of GCs, UCDs, and nuclei have red tails for all indices except $(i - z)_0$ for the nuclei. To quantify the bimodality of color distributions, we use Gaussian Mixture Modeling (GMM; Muratov & Gnedin 2010) and assume a homoscedastic distribution: i.e., two subpopulations having the same dispersions. As described by Muratov & Gnedin (2010), a dimensionless peak separation ratio D (see Equation A3 in their paper) should be larger than 2 for a bimodal distribution. We measure D for the color distribution in each panel of Figure 12. The D parameters for GCs and UCDs are larger than 2 while those for nuclei are

[28] The bimodal UCD color distribution for M49 reported in Liu et al. (2015a) has low statistical significance.

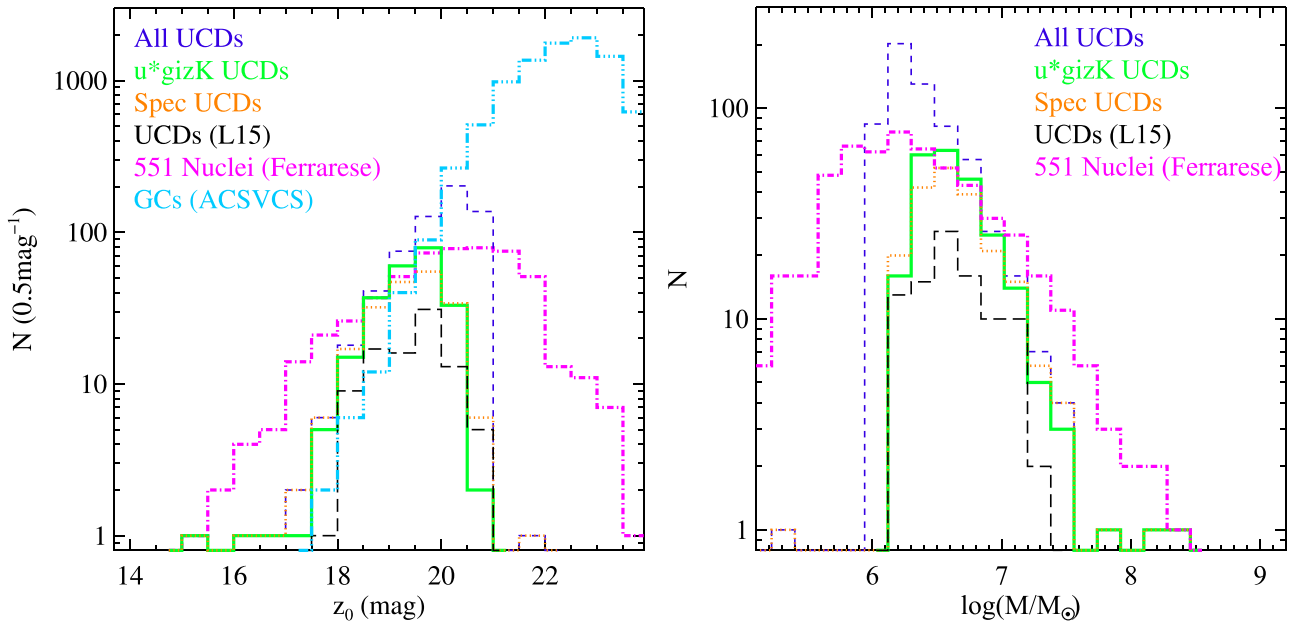

Figure 11. The distribution of z-band magnitudes (left panel) and stellar masses (right panel) for compact stellar systems in Virgo. Blue short-dashed line: `all UCDs` sample (612 candidates); green solid line: u^*gizK `UCDs` sample (235 candidates); orange dotted line: `spec UCDs` sample (203 candidates); black long-dashed line: 92 UCDs from Liu et al. (2015a); cyan line: `ACSVCS GCs` sample (Jordán et al. 2009); magenta line: `all nuclei` sample (Ferrarese et al. 2020).

smaller than 2. In addition, the unimodal distribution is rejected at a level better than 1% for `bright GCs` and better than 0.1% for `ACSVCS GCs` and u^*gizK `UCDs`.

The best-fit GMM models are shown in Figure 12 as well. For those distributions found to be bimodal, blue and red curves are used to represent the individual components (with vertical dashed lines marking their respective means), while the black curves represent their sums. Conversely, where unimodal distributions are favored, we show the best-fit Gaussians (black curves) and the corresponding means (vertical dashed lines).

In the case of a bimodal color distribution, GMM also yields the probability that a given object belongs to the blue or red component. We therefore calculate the fraction of objects belonging to the blue subpopulation, $f_{\rm blue}$. $f_{\rm blue}$, based on the $(g-z)_0$ color index, is 77% (±4%), 84% (±1%), and 89% (±3%) for `ACSVCS GCs`, `bright GCs`, and UCDs. Based on ACSVCS data, Peng et al. (2006b) concluded that the blue GC fraction for individual galaxies ranges from 85% to 40% and decreases with increasing host galaxy luminosity.

There are two main reasons why the blue fractions are different between `ACSVCS` and `bright GCs`. First, the blue fraction of `bright GCs` is calculated over the entire cluster that contains many more dwarf galaxies (which have higher $f_{\rm blue}$) than the ACSVCS galaxy sample. Second, as described in Jordán et al. (2005), almost all GCs in the Virgo cluster can be resolved in ACSVCS imaging, which enables a very clean GC selection (see Peng et al. 2006b; Jordán et al. 2009), while our `bright GC` sample is contaminated by many BGs when the K-band data are not available (see Table 1). Therefore, our `bright GC` sample contains more dwarf galaxies and is less pure than the `ACSVCS GC` sample, causing it to have a higher blue fraction. For nuclei, we can see from the last row of Figure 12 that the vast majority are blue with just a few having red colors. Because a unimodal distribution is preferred for this group, we are unable to calculate a blue fraction on the basis of GMM alone. However, considering that the blue and red components for GCs and UCDs cross at $(g-z)_0 \sim 1.1$, we can split the nuclei distribution at this color to calculate their blue fraction. In so doing, we find $f_{\rm blue} \sim 95\%$.

To summarize, for objects brighter than $g_0 = 21.5$, GMM fitting shows that GCs and UCDs exhibit bimodal color distributions while the nuclei follow a unimodal distribution with a small tail to red colors. Ordering these groups of compact stellar systems by $f_{\rm blue}$, from low to high, yields `ACSVCS GCs` < `bright GCs` $\lesssim$ UCDs < `bright nuclei`.

4.4. Size Distribution

In order to select UCDs, we have measured half-light radii for all bright objects ($g_0 < 21.5$) in the NGVS footprint using KINGPHOT. The left panel of Figure 13 plots $\langle r_h \rangle$ versus $(g-z)_0$ for our `all` (blue open circles), u^*gizK (green filled semicircles), and `spec UCDs` samples (orange filled semicircles), and `spec GCs` sample (cyan dots). It is worth noting that the majority of UCDs with very blue colors, $(g-z)_0 \lesssim 0.7$, lack radial velocity measurements, a situation we aim to improve upon through dedicated spectroscopic follow-up. The right panel shows the distribution of half-light radii for both UCDs and GCs. The dotted horizontal line marks $\langle r_h \rangle = 11$ pc, the size used to separate GCs from UCDs, while the dotted vertical line indicates the color, $(g-z)_0 = 1.1$, used to divide the UCDs into blue and red subpopulations (see Section 4.3).

The mean r_h of UCDs is $\overline{r_h} = 19.8$ pc with a standard deviation of $\sigma_{r_h} = 6.8$ pc. For subpopulations, the mean r_h and standard deviations are $\overline{r_h} = 20.0$ pc and $\sigma_{r_h} = 6.8$ pc for the blue UCDs, and $\overline{r_h} = 14.6$ pc and $\sigma_{r_h} = 3.8$ pc for the red UCDs. The blue UCDs are larger and cover a wider range in half-light radius than red ones.

As discussed in Liu et al. (2015a), when comparing to HST-based values, we find that we overestimate the half-light radii of smaller objects ($r_h \lesssim 11$ pc). Thus, we suspect that many diffuse GCs are included in our UCD sample. This may explain why we see such a high degree of similarity between the color distributions of our NGVS-based samples of GCs and UCDs.

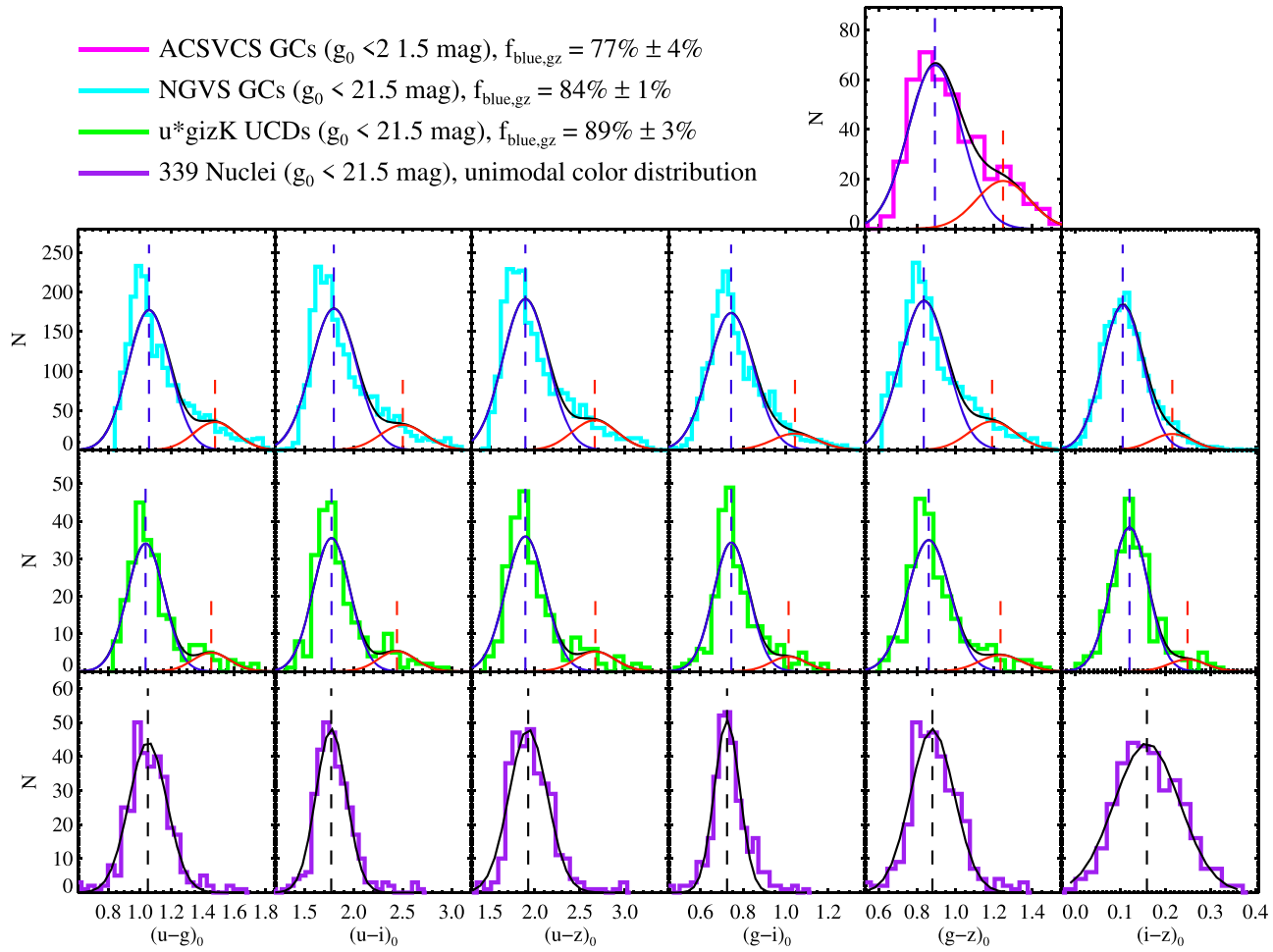

Figure 12. The color histograms for `ACSVCS GCs` (the first row, magenta histogram), `bright GCs` (the second row, cyan histograms), u^*gizK `UCDs` (the third row, green histograms), and `bright nuclei` (the fourth row, purple histogram). All objects are brighter than $g_0 = 21.5$ mag. Colors plotted, from left to right, are: $(u - g)_0$, $(u - i)_0$, $(u - z)_0$, $(g - i)_0$, $(g - z)_0$, and $(i - z)_0$. For the bimodal color distributions, we show blue and red Gaussian components (blue and red curves) and their sums (black curves). For the unimodal color distributions, we plot the best-fit single Gaussians using black curves. The vertical dashed line(s) shows the mean(s) of the associated color distribution(s).

At the time of writing, SMBHs have been detected in four Virgo UCDs. These objects (all of which were objectively identified by our selection function) are indicated by the large circles in the left panel of Figure 13). These are M60-UCD1 (Seth et al. 2014), M59cO (Ahn et al. 2017), VUCD3 (Ahn et al. 2017) and M59-UCD3 (Ahn et al. 2018). Interestingly, all four objects are quite red, with colors of $(g - z)_0 \sim 1.35$. Based on the color–magnitude relation for UCDs, we know that the redder systems tend to be brighter. To date, no blue UCD is known to contain a SMBH, although we have many promising bright, blue UCD candidates in our sample. These are obvious targets for future spectroscopic searches for SMBHs.

4.5. Subsamples of Unique UCDs

As noted above, we find no significant color differences between our UCD and GC samples. However, some UCDs, by virtue of their extreme or unusual properties, have a special significance for understanding the origin of these systems and their relationship to "normal" GCs. In this section, we pause to consider these unique UCDs.

4.5.1. The Brightest UCDs

We begin with the subset of UCDs that are known to contain an SMBH. The first such detection was made in M60-UCD1, where Seth et al. (2014) found a SMBH of mass $\sim 2.1 \times 10^7\, M_\odot$. The inferred mass fraction (15%) suggests that the progenitor of M60-UCD1 was a dwarf galaxy. Soon afterwards, an even more massive system in Virgo, M59-UCD3, was coreported by Liu et al. (2015b) and Sandoval et al. (2015). Later, Ahn et al. (2018) showed that this UCD also contains an SMBH of mass $4.2 \times 10^6\, M_\odot$. SMBHs have also been found in two more Virgo UCDs, M59cO and VUCD3 (Ahn et al. 2017). The discovery that UCDs can harbor SMBHs is crucial evidence of a dE, N origin for at least some UCDs.

One property that unifies the four UCDs with known SMBHs is their luminosity: they are all very bright. Based on this, we have carried out a search for bright UCDs using the NGVS short exposures. Figure 14 presents g-band cutouts for the nine brightest UCD candidates in our sample, which shows that M59-UCD3, M60-UCD1, and M59cO are the brightest three UCDs in all of Virgo, and the only three brighter than $g_0 = 18$ mag. The next brightest UCD, NGVS-UCD 761, with $g_0 = 18.74$ and $(g - z)_0 = 1.11$, represents a new detection and is a tantalizing target for future SMBH searches.

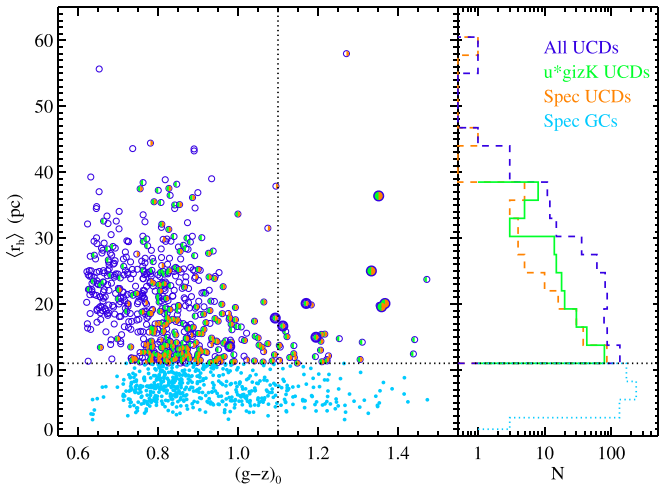

Figure 13. Left panel: mean half-light radius vs. $(g - z)_0$ color for `spec GCs` (cyan filled circles) and UCDs (`all UCDs`: blue open circles; u^*gizK `UCDs`: green filled semicircles; `spec UCDs`: orange filled semicircles). The four larger circles are those UCDs that are known to host SMBHs: i.e., M60-UCD1 (Seth et al. 2014), M59-UCD3 (Ahn et al. 2018), M59cO (Ahn et al. 2017), and VUCD3 (Ahn et al. 2017). The five thicker blue circles denote the five bright UCDS in Figure 14 that have not yet been studied for SMBHs. The vertical black dotted line shows the $(g - z)_0$ color, which is used to divide the GCs and UCDs into red and blue subpopulations. Right panel: r_h distribution for `all UCDs` (blue long-dashed line), u^*gizK `UCDs` (green solid line), `spec UCDs` (orange short-dashed line), and `spec GCs` (cyan dotted line). The horizontal black dotted line in both panels shows a half-light radius of 11 pc, which is used to separate UCDs from GCs.

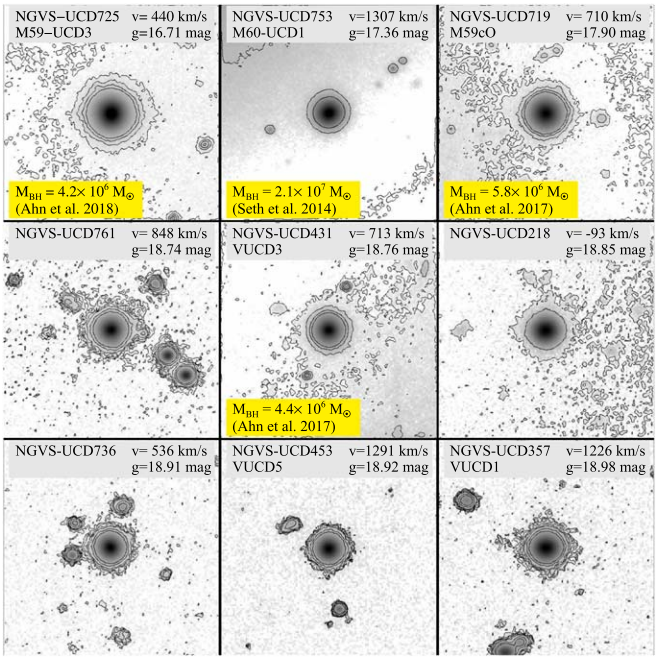

Figure 14. NGVS g-band images for the brightest nine UCDs in Virgo cluster. Radial velocities used to confirm cluster membership are available for each of these objects. Four of these UCDs are known to host SMBHs, the masses of which are reported in the panels. The image size in each panel is 120 × 120 pixels, where 120 pixels $\sim 22\farcs32 \sim 1.8$ kpc at Virgo distance.

Figure 15 shows the locations of the 23 UCDs in Virgo that are brighter than $g_0 = 19.5$ mag. The red stars represent the three brightest systems. We note that the third- (M59cO) and fourth-brightest UCDs (NGVS-UCD 761) are separated by a significant magnitude gap ($\Delta g_0 = 0.84$ mag). The fourth- ($g_0 = 18.74$ mag)

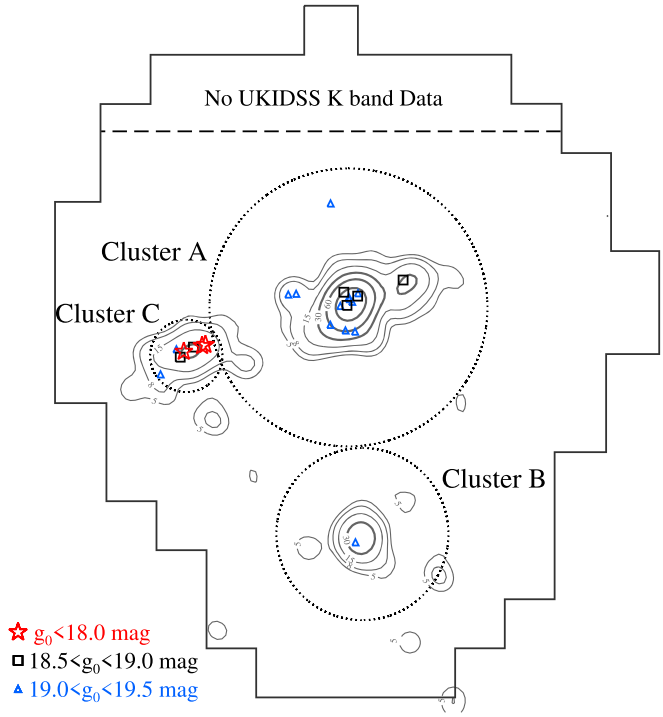

Figure 15. The spatial distribution of bright u^*gizK `UCDs` with $g_0 < 19.5$ mag. Red stars show the three UCDs with $g_0 < 18.0$ mag. Black squares show the six UCDs with $18.5 < g_0 < 19.0$ mag (note that there are no UCDs in the magnitude range $18.0 < g_0 < 18.5$ mag). Blue triangles show the 14 UCDs with $19.0 < g_0 < 19.5$ mag. Contours show the surface density distributions for the sample of 235 u^*gizK `UCDs` (see Figure 10). The large dotted circles show Virgo's three main subclusters: i.e., clusters A, B, and C, which are centered on M87, M49, and M60, respectively.

to ninth-ranked ($g_0 = 18.98$ mag) UCDs are shown as black squares in Figure 15, while blue triangles represent UCDs in the range of $19.0 < g_0 < 19.5$ mag.

Interestingly, all 23 UCDs with $g_0 < 19.5$ mag are located in Virgo's three main subclusters (black dotted circles). About half of these objects are in Cluster A (centered on M87)—4 with $18.5 < g_0 < 19.0$ and 11 $19.0 < g_0 < 19.5$. Curiously, the brightest three UCDs are all located in Cluster C, a much smaller subcluster centered on M60. On the contrary, only one bright UCD (ranked 20th; $g_0 = 19.39$) is found in Cluster B (centered on M49). It is puzzling why Cluster C is so special in this regard. Perhaps the fact that this substructure contains two massive galaxies in close proximity to one another makes it a conducive environment for forming bright UCDs (e.g., through tidal stripping).

4.5.2. The Largest UCDs

Figure 16 shows g-band cutouts for the nine largest UCDs in our sample. The largest, NGVS-UCD 769 ($\langle r_h \rangle = 58$ pc.[29]), also happens to be the brightest ($g_0 = 19.11$ mag) and reddest one ($(g - z)_0 = 1.27$) of this subsample; the remaining eight all have $(g - z)_0 \lesssim 1.1$. There is, interestingly, no overlap between the nine brightest and nine largest UCDs in our sample. Only two of the largest UCDs currently have measured radial velocities.

We note that three UCDs in Figure 16 (NGVS-UCD 549, 506 and 757) have bright neighbors. Recall that when we

[29] Note that the largest nucleus in Virgo has $r_h \sim 60$ pc (Côté et al. 2006).

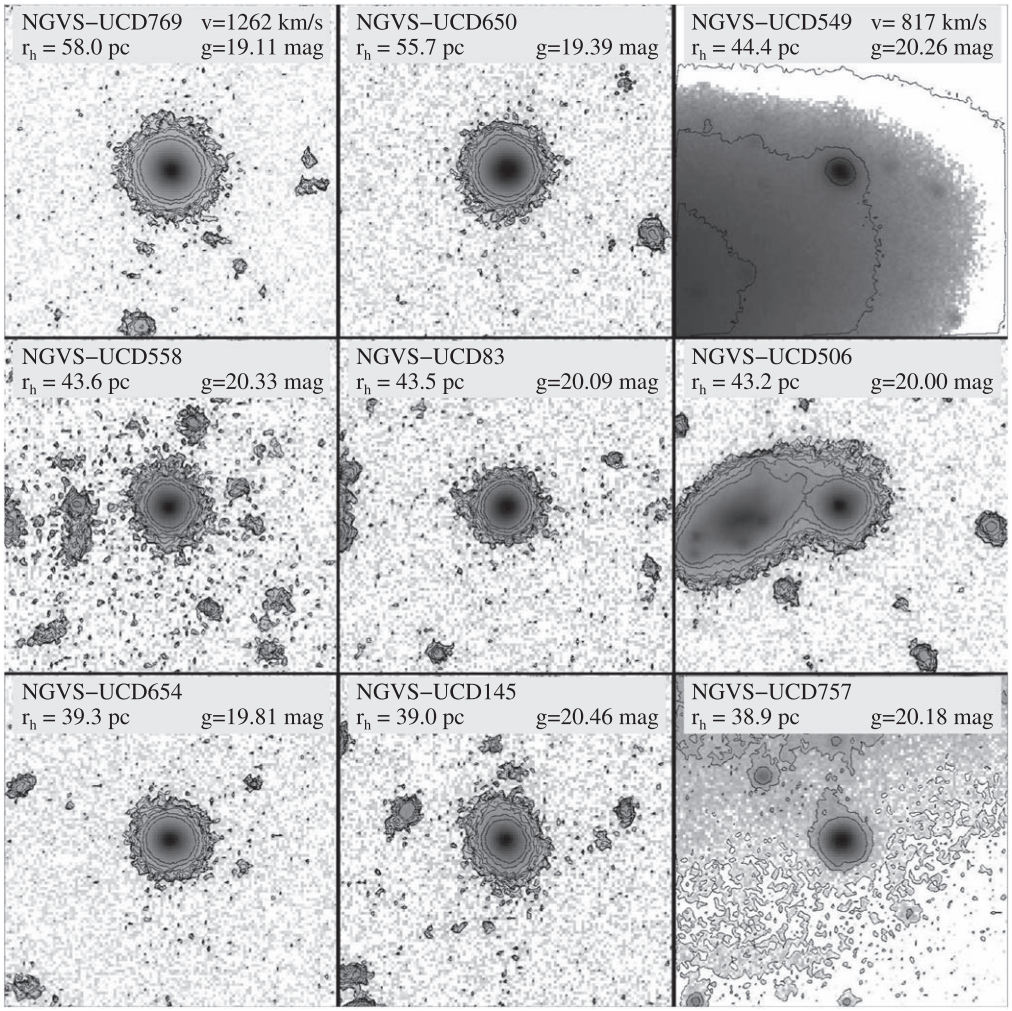

Figure 16. NGVS *g*-band images for the largest nine UCDs in Virgo cluster. The image size in each panel is 120 × 120 pixels, where 120 pixels $\sim 22\farcs32 \sim 1.8$ kpc at the distance of Virgo.

measure the half-light radius of an object, KINGPHOT fits the image using PSF-convolved King models within a fitting radius $r_{\rm fit}$ (15 pixels here). In Figure 3, we compare r_h measurements based on different fitting radii, $r_{\rm fit} = 7$ or 15 pixels. The measurements are fully consistent even for the UCDs surrounding the three most luminous galaxies in the Virgo cluster (M87, M49, and M60). We conclude then that light from neighboring galaxies does not seriously affect our r_h measurements. In addition, we test our measurement procedure by injecting artificial UCDs across a range of environments covered by the NGVS footprint. We find that the KINGPHOT measurements are quite robust unless the UCD falls very close to a bright point source, like the blended objects shown in Figure 8.

Using the ACSVCS data, Jordán et al. (2005) found that the vast majority of GCs in the Virgo cluster are smaller than $r_h = 10$ pc, with their average size being $\langle r_h \rangle = 2.70 \pm 0.35$ pc. In addition, they found no correlation between half-light radius and luminosity for `bright GCs` ($z \leqslant 22.9$ mag). Meanwhile, using ACSVCS data as well, Côté et al. (2006) found that nuclei follow a size–magnitude relation, with more luminous nuclei having larger half-light radii. A similar result has been found for UCDs, although not as tight (i.e., more luminous UCDs are usually larger; Côté et al. 2006; Penny et al. 2014). Dabringhausen et al. (2012) have also reported that UCDs follow a size–magnitude relation, while GCs do not.

It is worth pointing out that several GCs in our MW are also larger than $r_h = 10$ pc (van den Bergh & Mackey 2004). Such extended star clusters (ESCs) have also been found around other nearby galaxies, e.g., M31 (Huxor et al. 2005, 2014), ScldE1 (Da Costa et al. 2009), M51 (Hwang & Lee 2008), and NGC 6822 (Hwang et al. 2011). These ESCs mainly populate the faint end of the GCLF (Peng et al. 2006a; Liu et al. 2016), with those around the MW and M31 being fainter than $M_V = -7$ (van den Bergh & Mackey 2004; Hwang et al. 2011). Conversely, the typical UCD is brighter than ESCs by two magnitudes or more ($-13 < M_V < -9$ mag; Willman & Strader 2012), and by more still for the largest UCDs. Therefore, it is quite likely that the largest UCDs in Virgo originate under different circumstances than "normal" GCs.

4.5.3. UCDs with Asymmetric/Tidal Features

If tidal stripping of dE, Ns produce UCDs, then we should be able to find some objects undergoing such a transformation (i.e., UCDs that exhibit asymmetries and/or tidal features). Of course, this exercise may be complicated by short transformation timescales and/or potentially low surface brightnesses of any stripped material (Pfeffer & Baumgardt 2013). Nonetheless, a

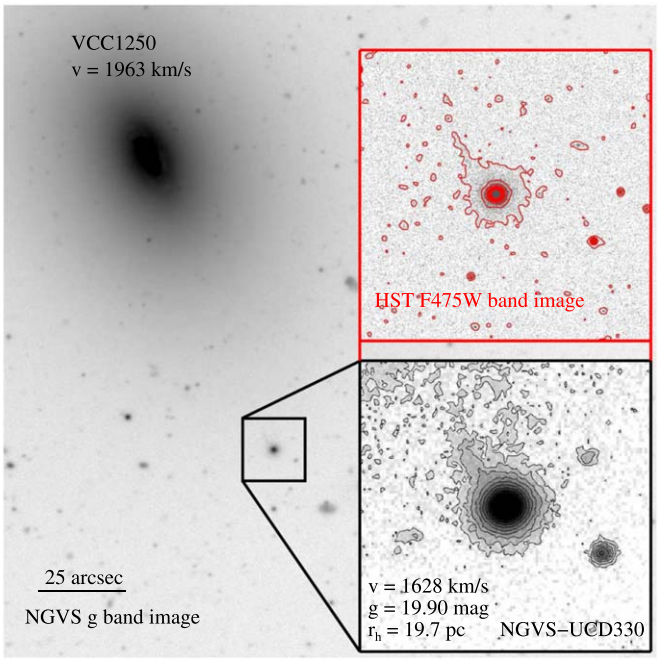

Figure 17. NGVS g-band image for galaxy VCC 1250. The small panels shows the NGVS and HST images of NGVS-UCD 330, a UCD that shows signs of an extratidal structure. The inset image with red contours is taken from the HST ACS Virgo Cluster Survey.

few UCDs with asymmetric or tidal features have indeed been found in recent years through deep surveys (e.g., Jennings et al. 2015; Mihos et al. 2015; Voggel et al. 2016; Schweizer et al. 2018). Another potential complication surrounds the interpretation of such features—for instance, several GCs around the MW are known to possess prominent tidal structures, such as NGC 6715 (Ibata et al. 1994; Bellazzini et al. 2008), Palomar 5 (Odenkirchen et al. 2001), and ω Cen (Ibata et al. 2019). However, most of these objects have been flagged by other studies as unusual members of the MW GC system (Johnson et al. 2015; Milone et al. 2017; Gratton et al. 2019), such that they are commonly held as remnants of nucleated satellites that were disrupted by the MW's tidal field (e.g., Bekki & Freeman 2003; Majewski et al. 2003; Küpper et al. 2015).

The high sensitivity of the NGVS images ($\mu_g \lesssim 29$ mag arcsec^{-2}; Ferrarese et al. 2012) allows us to search for such features within our UCD sample. Our search indeed results in a handful of UCDs with apparent asymmetries. If confirmed as being tidal in origin, these features would offer direct evidence that at least some UCDs are the descendants of nucleated galaxies.

Figure 17 shows one candidate tidal structure associated with NGVS-UCD 330. This UCD ($v_r = 1628$ km s^{-1}) is a satellite of VCC 1250 ($v_r = 1963$ km s^{-1}). It was previously identified as VCC 1250_1 by Haşegan et al. (2005), who also noted that it appeared to be embedded in a diffuse envelope. Both the NGVS and HST images in Figure 17 reveal an asymmetric structure emanating from this object and pointing toward VCC 1250. Thus, NGVS-UCD 330 may be an example of a UCD caught in the act of losing what remains of its diffuse envelope. The putative tidal stream associated with this UCD is unusual in that we only detect one arm. However, we cannot rule out the second arm as being hidden by projection or surface brightness effects. Follow-up spectroscopy of this object would help us determine its origins.

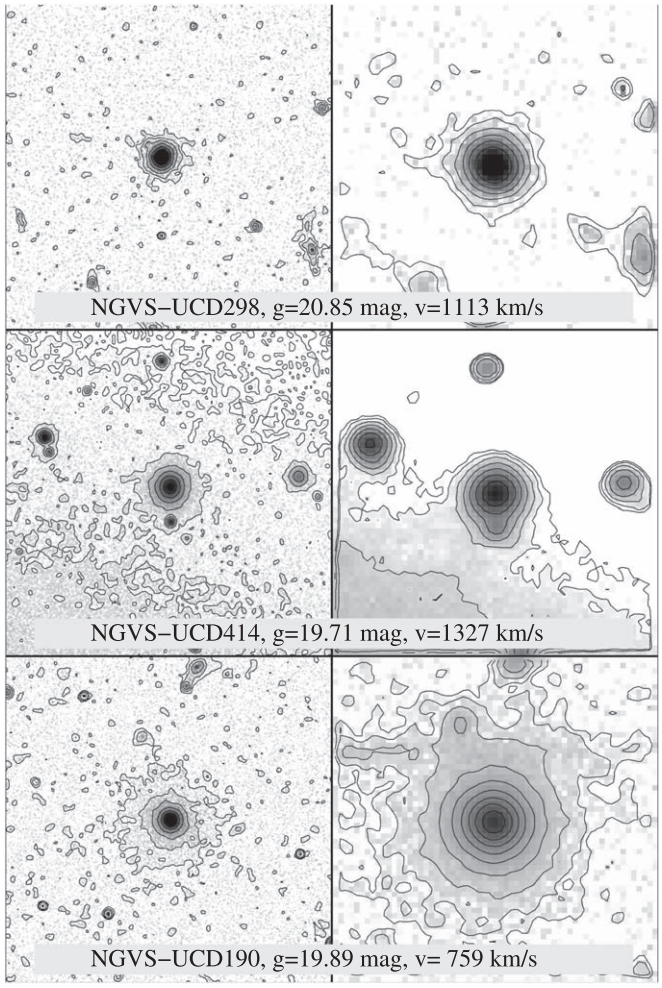

Figure 18. HST F475W (∼SDSS g-band) images (left panels) and NGVS g-band images (right panels) for the UCD candidates, NGVS-UCD 298, 414, and 190 (from top to bottom panels). Each of these objects are confirmed radial velocity members of the Virgo cluster (i.e., $v_r < 3500$ km s^{-1}). The image size in each panel is ∼0.9 kpc × 0.9 kpc.

4.5.4. UCDs with Envelopes

Using HST imaging, Haşegan et al. (2005) found three UCDs in Virgo that are embedded within shallow envelopes—evidence that they may be related to the nuclei of dE, Ns with extremely low surface brightness and/or compact stellar halos. There are 22 UCD candidates in our sample that also have HST imaging from the ACSVCS (Côté et al. 2004). We have checked these HST images to look for envelopes. Some systems, like NGVS-UCD 298 (top panel of Figure 18), show no evidence of envelopes in either the ACSVCS or NGVS images. Others, like NGVS-UCD414 (middle panel of Figure 18), have small envelopes that are visible only in the ACSVCS images thanks to its exceptional image quality. The remainder, like NGVS-UCD 190 (bottom panel of Figure 18), have large (yet still diffuse) envelopes that can be seen in both ACSVCS and NGVS images. In all, we find about half of the 22 UCD candidates with HST imaging are embedded in diffuse envelopes that are visible in space-based images.

The above comparison demonstrates that we can detect envelopes around UCDs in the NGVS imaging, provided they

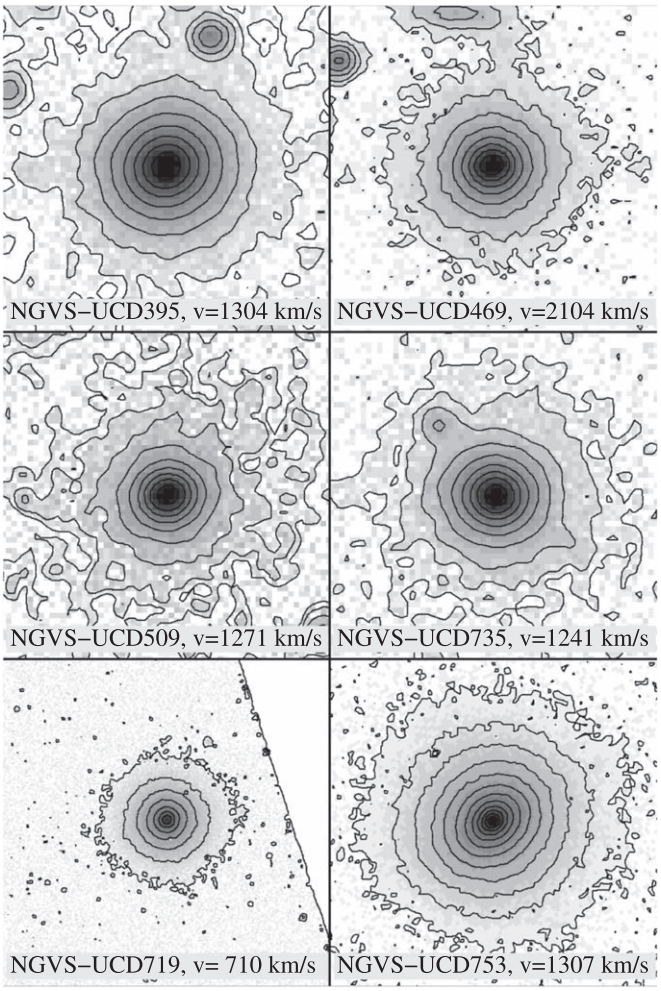

Figure 19. NGVS *g*-band images for four UCDs (upper four panels) and HST F475W (∼SDSS *g* band) images for two UCDs (lower two panels) having visible envelopes. Each of these objects are confirmed radial velocity members of the Virgo cluster (i.e., $v_r < 3500$ km s^{-1}). The image size in each panel is the same as in Figure 18.

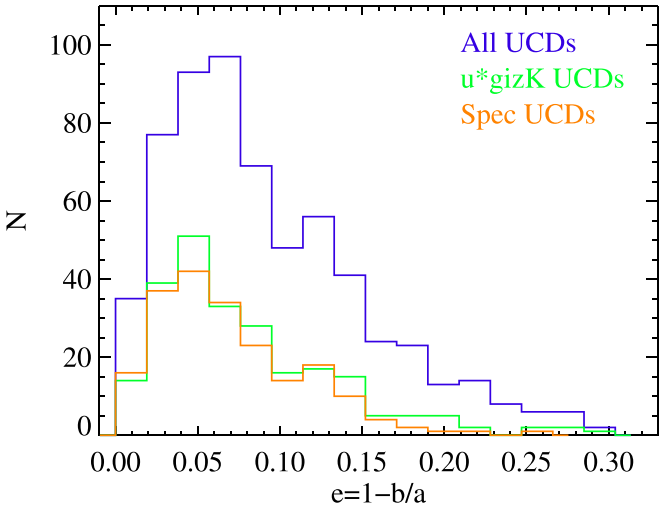

Figure 20. The ellipticity distributions of `all UCDs` (blue histogram), u^*gizK–`UCDs` (green histogram), and `spec UCDs` sample (orange histogram).

are large enough. Our search reveals 41 instances of such features, and these cases have been flagged accordingly in Table 4. Most of these UCDs are found around M87 and M60/M59, with just a couple located in subcluster B. Note that, in this section, we have focused on UCDs with envelopes that are obvious based on visual inspection, which is admittedly subjective. Because this sample is not suitable for statistical analysis, we will postpone the detailed investigation of the properties of UCD envelopes to future work (K. Wang et al. 2020, in preparation). In the next section though we will introduce a parameter, $\Delta_{\rm env}$, to examine basic properties of the envelope.

Figure 19 presents NGVS *g*-band images for four UCDs (upper four panels) and HST F475W (∼SDSS *g*-band) images for two UCDs (lower two panels) that are confirmed radial velocity members of the Virgo cluster and possess clear stellar envelopes. We see in both sets of imaging that these envelopes have near-zero ellipticity. From a morphological perspective, UCDs with diffuse envelopes look quite similar to dE, Ns, adding weight to the argument of an evolutionary connection between the two classes. Moreover, NGVS-UCD 719 (lower-left panel of Figure 19, also known as M59cO; Chilingarian & Mamon 2008) and NGVS-UCD 753 (lower-right panel of Figure 19, also known as M60-UCD1; Strader et al. 2013) are two of the four UCDs known to possess central SMBHs (Seth et al. 2014; Ahn et al. 2017). We do not, however, observe any tidal features around them (e.g., Küpper et al. 2010; Jennings et al. 2015; Schweizer et al. 2018).

As with tidal features, the interpretation of envelopes around Virgo UCDs is also potentially complicated by the fact that similar structures have recently been detected around the MW GCs NGC 7089 (Kuzma et al. 2016) and NGC 1851 (Kuzma et al. 2018). Once again though, these GCs are unusual in their chemistries (e.g., possessing broad dispersions in their abundances of iron and neutron-capture elements; Johnson et al. 2015; Milone et al. 2017), suggesting that they are actually the remnant nuclei of disrupted nucleated galaxies.

5. Discussion

We have selected candidate Virgo UCDs from a combination of ellipticity, magnitude, colors, surface brightness, half-light radii, visual inspection, and when available, radial velocity. At the outset, we imposed a requirement that ellipticity $e < 0.3$ because most spectroscopically confirmed UCDs are quite round (Zhang et al. 2015). We show the ellipticity distributions of our UCD samples in Figure 20 to gauge the impact this has on our selection function. As can be seen, the ellipticity distributions peak at ∼0.05–0.07 and decrease to roughly zero by $e \approx 0.3$. We conclude then that the criterion $e < 0.3$ does not significantly bias our selection of UCDs.

Our selection yields a catalog of more than 600 candidates within the ∼100 deg^2 footprint of the NGVS, making it the largest and most homogeneous UCD catalog for any environment to date. Moreover, our selection algorithm also produces samples of `bright GCs` and galactic nuclei, such that we can compare directly the properties of these different populations.

Our large and complete sample also makes it possible to identify groups of UCDs with extreme or interesting properties, which may shed light on UCD origins in general. In this section, we examine our results using both approaches and discuss the implications for models of UCD formation.

We begin by noting that the nuclei of dwarf galaxies are embedded in stellar envelopes that can vary widely in surface brightness (see, e.g., Ferrarese et al. 2006; Spengler et al. 2017;

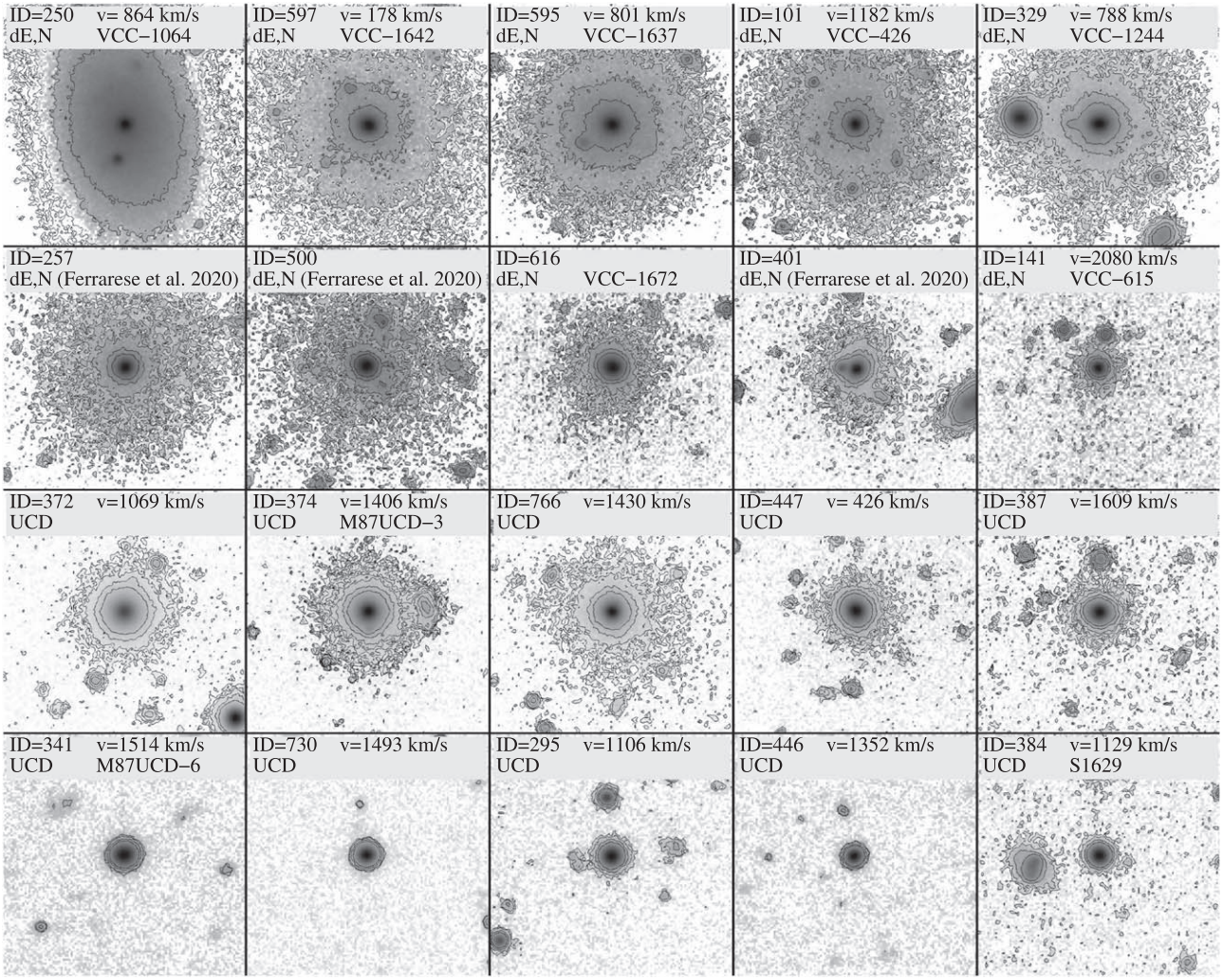

Figure 21. Mosaic of g-band images for 20 objectively selected UCD candidates from the NGVS. The image size is 120 × 120 pixels (where 120 pixels = 22.″32 ∼ 1.8 kpc in Virgo cluster). The upper row shows five nucleated dwarf galaxies (dE, N) from the VCC catalog (Binggeli et al. 1985). All of them are confirmed spectroscopic members of the Virgo cluster (i.e., $v_r < 3500$ km s^{-1}). Another five dE, Ns shown in the second row include two VCC galaxies (ID = 613 and 141) and three newly discovered galaxies from the NGVS (ID = 257, 497, and 401; Ferrarese et al. 2020). Four of these five dE, Ns do not have radial velocity measurements, but they are likely cluster members given their extended, low-surface-brightness envelopes. The rightmost galaxy in this row (ID = 141) is an ultradiffuse galaxy that has a large extent (larger than the figure size) and very diffuse structure (e.g., Toloba et al. 2018). The third row shows five UCDs with apparent envelopes while the bottom row shows another five UCDs that have no discernible envelope. All 10 UCDs are radial velocity members of the cluster ($v_r < 3500$ km s^{-1}). The contours in each of the first 15 panels show the isophotes with constant surface brightness level. The innermost isophote is 25 mag arcsec^{-2}, and each interval between successive isophotes is 0.5 mag arcsec^{-2}. The 10 dE, Ns (the top two rows) have been sorted by the size of the stellar halo, while the UCDs (the bottom two rows) by the envelope parameter, $\Delta_{\rm env}$.

Toloba et al. 2018). In other words, when we visually classify our UCD candidates, it can be difficult to distinguish UCDs with faint envelopes from nuclei in low-mass galaxies. To solve this, we remove from our samples any objects that have been classified as galaxies in either the VCC (Binggeli et al. 1985) or the NGVS galaxy catalogs (Ferrarese et al. 2016, 2020).

Figure 21 shows a mosaic of NGVS g-band images for representative subsamples of 10 dE, Ns and 10 UCDs. Most of these objects are confirmed radial velocity members of Virgo. Note that this mosaic is an updated version of Figure 32 in Liu et al. (2015a), which was based on just ∼100 UCD candidates near M87 and that the dE, Ns have been sorted by the prominence of their stellar envelopes. We can see that the envelopes of the first few dwarfs are significant, making it easy to identify these systems as galaxies. However, as the envelopes become progressively smaller and fainter, the distinction between dE, Ns and UCDs becomes blurred. For instance, it is difficult to distinguish the dE, Ns in the second row of Figure 21 from the UCDs in the third row, based on morphology alone. Note that the systems in the second row are classified as galaxies in either the VCC (ID = 613 and 141, Binggeli et al. 1985) or NGVS galaxy catalogs[30] (Ferrarese et al. 2016, 2020; Sánchez-Janssen et al. 2019). Finally, as the bottom row of Figure 21 illustrates, most of our UCD candidates do not have visible envelopes, or they are too diffuse to detect with NGVS imaging.

Figure 21 prompts an obvious question: might there be an evolutionary sequence that links dE, N galaxies to UCDs, with the latter representing the end state of severe and continuous tidal stripping? Such a link was suggested by Liu et al. (2015a), who examined the distribution of dwarf galaxies and UCDs in the cores of the Virgo A and B subclusters. Armed with a

[30] Of course, in both of these catalogs, galaxy classifications were based on several properties, not just morphology.

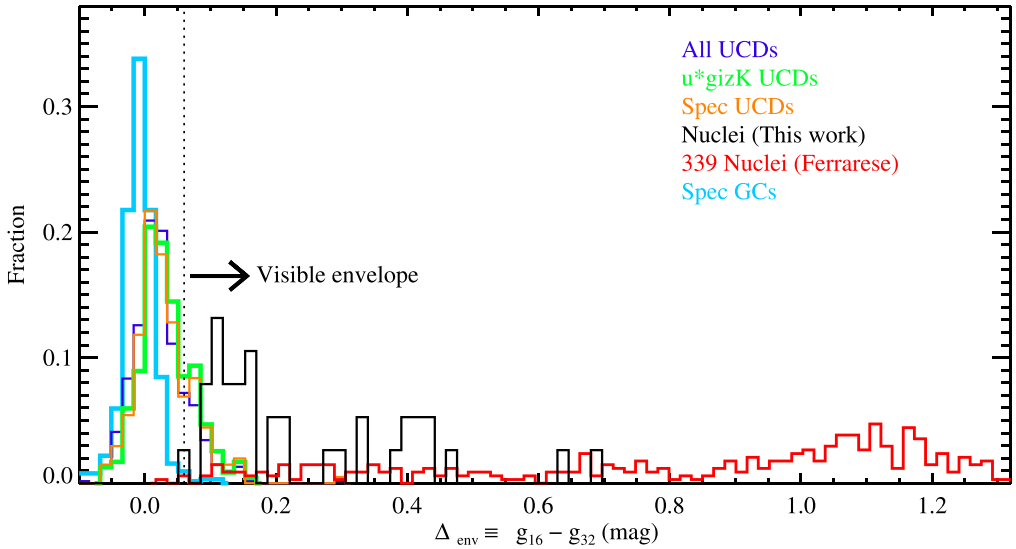

Figure 22. The envelope parameter, $\Delta_{\rm env}$, distribution for the `spec GCs` (cyan), `all UCDs` (blue), u^*gizK `UCDs` (green), `spec UCDs` (orange), u^*gizK `nuclei` (black), and `bright nuclei` (red). We have divided the UCDs into two subgroups at $\Delta_{\rm env} = 0.06$, shown by the dotted vertical line.

clusterwide sample of UCDs and galaxies, we can now revisit this claim. Bekki & Yong (2012) found from their numerical simulations a morphological sequence similar to that shown in Figure 21 (see the lower panel of their Figure 2). During the transformation from a dwarf galaxy to a bare nucleus, they showed that the stellar halo is stripped efficiently and decreases in size steadily over time. In other words, the physical extent of a given UCD envelope may indicate which stage the system falls along the evolutionary sequence from dE, N to UCD.

To further explore such a connection, Liu et al. (2015a) introduced a parameter to describe the strength of a UCD's envelope. This parameter is defined as $\Delta_{\rm env} \equiv g_{16} - g_{32}$, where g_{16} and g_{32} are g-band magnitudes measured within apertures of 16 ($\sim 3\farcs0$) and 32 pixels ($\sim 6\farcs0$) diameter, respectively. Based on this definition, pointlike sources should have $\Delta_{\rm env} \simeq 0$ while extended sources will tend to have $\Delta_{\rm env} > 0$.

Figure 22 shows the distribution of envelope parameters for compact objects in the NGVS. The GCs are closely distributed around $\Delta_{\rm env} \sim 0$, with a small tail to $\Delta_{\rm env} > 0.06$ (marked by the dotted vertical line). The low envelope strengths of GCs are to be expected given that the vast majority of them are unresolved in NGVS imaging. Meanwhile, the dE, Ns show much larger envelope strengths ($\Delta_{\rm env} > 0.06$). For UCDs, the envelope strengths typically fall between those of GCs and dE, Ns. Following Liu et al. (2015a), we subdivide the UCDs into two groups at $\Delta_{\rm env} = 0.06$. UCDs with $\Delta_{\rm env} > 0.06$, whose envelopes are clearly evident, more closely resemble nuclei and are thus distinct from GCs.

Previous studies have found dramatic differences in the cumulative radial distributions of UCDs and dE, Ns in galaxy clusters (e.g., Drinkwater et al. 2002, 2004; Mieske et al. 2004b, 2007a; Jones et al. 2006; Liu et al. 2015a; Pfeffer et al. 2016), but the situation between UCDs and GCs is less clear (e.g., Mieske et al. 2004a, 2012). Generally, GCs are highly concentrated toward cluster centers, while dE, Ns are less concentrated and UCDs lie intermediate between the two. If the majority of UCDs are nothing more than the high-luminosity tail of the GC population, then we might reasonably expect the radial distributions of GCs and UCDs to resemble each other. On the other hand, if most UCDs form through tidal stripping of dE, Ns, then we should expect the UCD radial profile to have a high central concentration: i.e., stripped galaxies would tend to lie deeper in the gravitational wells of their hosts. As noted in Section 4, our UCD sample most certainly contains some number of GCs because bright, extended GCs (although rare) do exist and we systematically overestimate the sizes of GCs. We can, however, invoke $\Delta_{\rm env}$ to produce a UCD sample that is more heavily weighted to objects born of tidal stripping.

The right panel of Figure 23 shows the cumulative radial distribution of UCDs, `bright GCs` (cyan lines), and `bright nuclei` (red lines) in the core of subcluster A ($D_{\rm M87} < 20R_{e,\rm M87}$). Here, we separate the UCDs into two groups: those without ($\Delta_{\rm env} \leqslant 0.06$; brown line) and those with ($\Delta_{\rm env} > 0.06$; purple line) envelopes. Consistent with previous studies, the ordered sequence of systems from high to low concentration in this region goes: GCs, UCDs without envelopes, UCDs with envelopes, and dE, Ns. As expected, the UCDs with envelopes are less centrally concentrated than those without. The difference in radial distributions between GCs and UCDs with $\Delta_{\rm env} > 0.06$ is clear.

In the left panel of Figure 23, we show, for the first time, the radial distribution of UCDs, GCs, and nuclei over the entire Virgo cluster. In the outer regions, the distributions of `bright GCs` and dE, Ns grow at similar rates. This makes sense because, at large clustercentric distances, GCs will be found around the individual galaxy members. On the other hand, there is a clear difference in how bright GCs and UCDs with envelopes are distributed in the outskirts of the cluster. Most notably, the distribution of UCDs with envelopes exhibits clear bumps that coincide with the locations of the three luminous galaxies, M86, M60, and M49 (marked by the black vertical lines). This indicates that the UCDs with envelopes are mainly associated with giant galaxies, where the gravitational potential is deep enough to strip the diffuse components of dE, Ns.

Another way we can attempt to isolate those UCDs formed via tidal stripping is by increasing the value of our size cut to $r_h > 20$ pc. On the right-hand panels of Figure 24, we examine the color–magnitude relations of UCDs with $\Delta_{\rm env} > 0.06$ or $r_h > 20$ pc and compare them to those for the `bright GCs` (upper-right panel) and `bright nuclei` (lower-right panel). Meanwhile, the left-hand panels show a similar comparison, but using our u^*gizK `UCDs` sample instead. Placing more

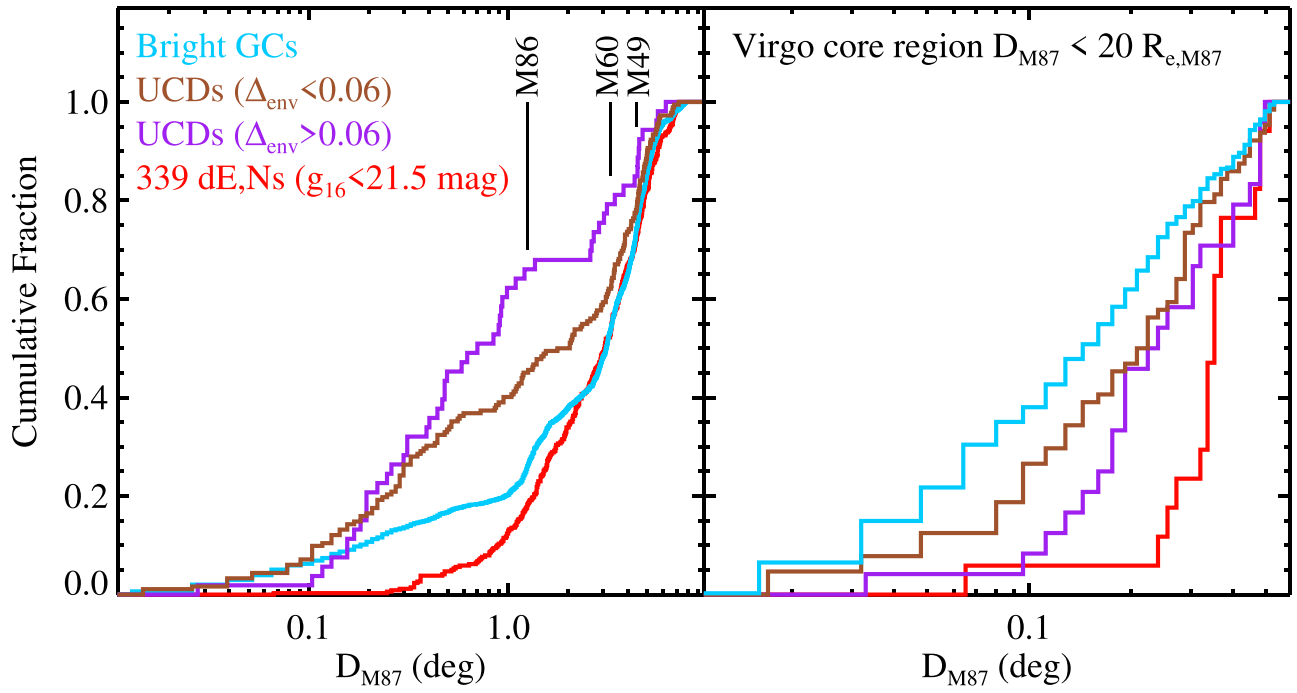

Figure 23. Cumulative distributions for the projected distance from M87 (D_{M87}) for the `bright GCs` (cyan lines), UCDs with $\Delta_{env} < 0.06$ (brown lines), UCDs with $\Delta_{env} > 0.06$ (purple lines), and `bright nuclei` (red lines). Left panel: the distribution for the entire NGVS survey area. Right panel: the distribution for the Virgo core region (within 20 $R_{e,M87}$). The three black vertical lines in the left panel show the location of M86, M60, and M49.

restrictive cuts on r_h and Δ_{env} has the effect of removing many red UCDs at faint luminosities ($z_0 \gtrsim 18.5$ mag). The color–magnitude relation for the u^*gizK `UCDs` sample is

$$(g - z)_0 = -0.12(\pm0.01)z_0 + 3.13(\pm0.05), \quad (8)$$

while that for our more restricted UCD sample is

$$(g - z)_0 = -0.13(\pm0.01)z_0 + 3.35(\pm0.04), \quad (9)$$

which are shown as blue solid lines in Figure 24.

At face value, it looks like the distributions of UCDs and nuclei overlap well in the color–magnitude plane. This compares well with previous work (e.g., Côté et al. 2006; Brodie et al. 2011), which found general agreement between the color–magnitude relations of nuclei and UCDs, in the sense that brighter UCDs and nuclei tend to be redder. However, as seen in the lower-right panel of Figure 24, there is a lack of blue UCDs at bright magnitudes ($z_0 \lesssim 18.0$) and that UCDs are bluer than nuclei at faint magnitudes ($z_0 \gtrsim 18.0$). To evaluate the significance of these differences, we have run a 2D Kolmogorov–Smirnov Test (Peacock 1983; Fasano & Franceschini 1987) on the distributions for UCDs and nuclei. The resulting p-values are quite small, implying that the distributions do not share a common parent. Also, in agreement with previous work (e.g., Brodie et al. 2011), we find that UCDs occupy a narrower range of color than GCs, especially at faint magnitudes. The color–magnitude relations of UCDs, nuclei, and GCs are thought to be the result of an underlying mass–metallicity relation for each population, with more massive systems tending to have higher metallicities and GCs tending to have higher metallicities than UCDs and nuclei at a given mass (especially at low masses; Zhang et al. 2018).

As described in the introduction, recent studies are finding more support for the galactic nuclei origin for UCDs. For UCDs formed this way, one would expect to find some transition objects: e.g., UCDs with tidal streams. However, only a small number of UCDs have been found to show such tidal structures (e.g., Figure 17, Jennings et al. 2015; Mihos et al. 2015; Voggel et al. 2016; Schweizer et al. 2018). On the other hand, many more UCDs were found to show diffuse, but circular, envelopes as shown in Figures 19, 21 and also previous studies (e.g., Drinkwater et al. 2003; Haşegan et al. 2005). Bekki & Yong (2012) have established that diffuse and circular envelopes can indeed be found around nuclei when the stellar halos of dwarf galaxies have been mostly stripped by tidal forces. Pfeffer & Baumgardt (2013) have also demonstrated that while the stellar halos of dwarf galaxies are reduced during the tidal stripping, they can still be visible at later stages, especially for the more massive and extended UCDs. By contrast, tidal streams are often much fainter and only can be observable for those UCDs that are still experiencing significant stripping.

Two decades have passed since the discovery of UCDs, and yet, we still lack an understanding of what fraction of them originate through the formation of GC systems versus tidal stripping. One of the chief reasons for this is the difficulty of identifying a given compact stellar system as a bare nuclear star cluster based on its integrated light. More locally, though, following years of study using high-resolution spectroscopy and resolved photometry, we now know that the GC system of the MW includes several unusual objects. These anomalous GCs tend to have very high surface mass densities, large intrinsic metallicity dispersions, spreads in the abundances of s-process elements, complex subgiant branches, kinematic subpopulations, and tidal streams (see the review of Gratton et al. 2019 and references therein). Many of these (massive) GCs are thought to be remnants of nucleated dwarf galaxies (e.g., M54, Ibata et al. 1994; ω Cen, Bekki & Freeman 2003) and thus can be considered local examples of UCDs.

Beyond the Local Group, however, there is no consensus definition for what is a UCD. Investigators typically base their

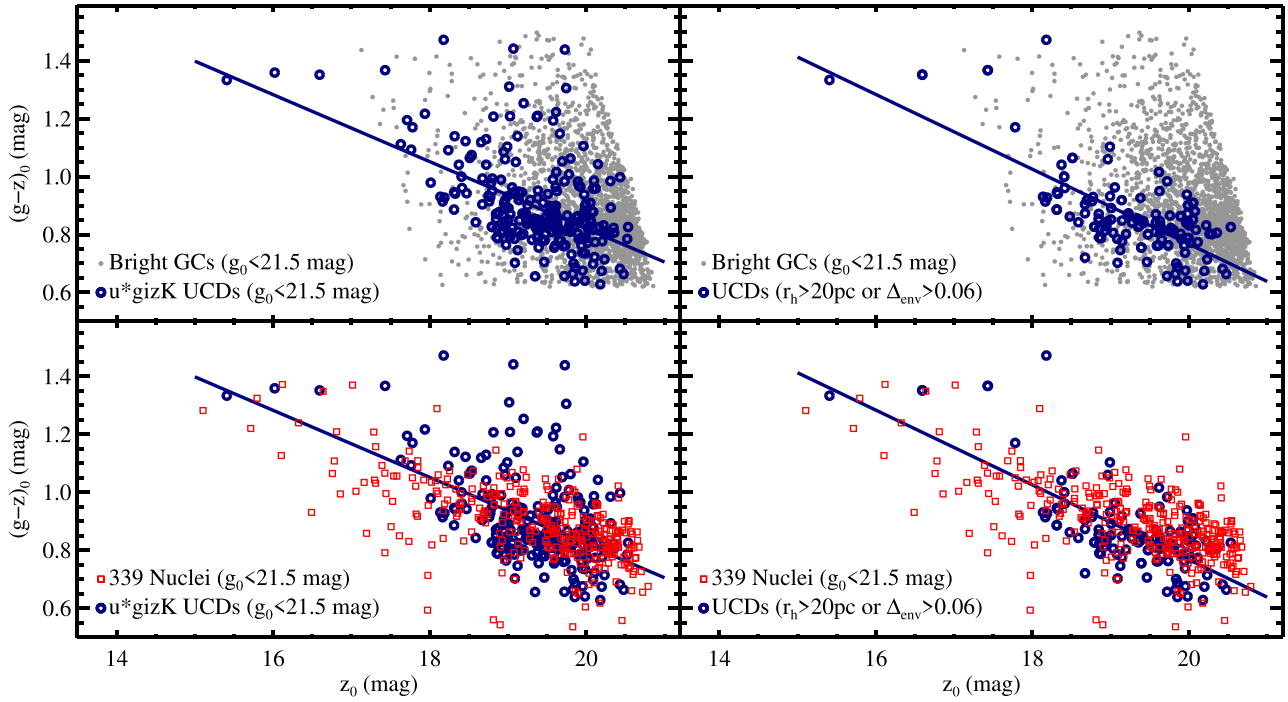

Figure 24. Color–magnitude diagram (CMD) for `bright GCs` (gray points), UCDs (blue open circles), and `bright nuclei` (red open squares). Upper-left panel: CMDs for `bright GCs` and u^*gizK `UCDs`. Lower-left panel: CMDs for `bright nuclei` and u^*gizK `UCDs`. Upper-right panel: CMDs for `bright GCs` and UCDs with $r_h < 20$ pc or $\Delta_{\rm env} > 0.06$. Lower-right panel: CMDs for `bright nuclei` and UCDs with $r_h < 20$ pc or $\Delta_{\rm env} > 0.06$. The blue solid lines in the left two panels are the best linear fit for u^*gizK `UCDs`. The blue solid lines in the right two panels are the best linear fit for UCDs with $r_h < 20$ pc or $\Delta_{\rm env} > 0.06$.

selection on arbitrary size ($10 \lesssim r_h \lesssim 100$) and luminosity/mass cuts ($10^6 \lesssim M_* \lesssim 10^8\,M_\odot$), or simply observational limits (e.g., $r_h > 11$ pc in this study). As a result, it is very challenging to isolate within current UCD samples those that are GC-like from those that are nuclei-like, as discussed by Hilker (2011). Nevertheless, recent work makes it clear that many UCDs (e.g., massive UCDs, UCDs with tidal structures or diffuse envelopes) are indeed the nuclei of stripped dwarfs. Moreover, based on the Guo et al. (2011) semianalytic model, Pfeffer et al. (2014) have demonstrated that both massive GCs ($M_* \gtrsim 10^5\,M_\odot$) and UCDs can form via tidal disruption of dwarf galaxies. Also, R. J. Mayes et al. (2020, in preparation) use the EAGLE simulation suite (Crain et al. 2015) to show that there is overlap between stripped nuclei and "normal" GCs in the stellar mass range $M_* \lesssim 2 \times 10^6\,M_\odot$.

To date, there are $\sim 10^3$ known UCDs in the local universe, more than half of which were found on the basis of photometric data alone. Obtaining spectroscopic observations for larger samples of UCDs (to measure radial velocities, velocity dispersions, and stellar populations) will be essential for understanding their nature. Fortunately, the next generation of ground- and space-based observatories promise to ameliorate this current deficit.

6. Summary and Conclusions

Using deep, wide-field u^*, g, i, z imaging from the NGVS and K-band data from the UKIDSS, we have carried out a systematic search for UCDs across the entire Virgo cluster ($\sim$104 deg^2). We describe our search methodology—which is based on a combination of photometric (magnitude and color) information, half-light radius and surface brightness measurements, and radial velocity measurements, when available—and present a sample of 612 UCD candidates. Among this UCD sample are 235 candidates selected on the basis of deep u^*gizK data (our highest purity subsample) and 203 UCDs that are confirmed radial velocity members of the cluster (i.e., $v_r < 3500\,{\rm km\,s^{-1}}$). This is the largest and most homogeneous sample of UCDs presented to date for any cluster environment, and the first of its kind for the Virgo cluster. Our principal findings can be summarized as follows:

1. We construct the first number density map for UCDs in the Virgo Cluster and show that UCDs are highly concentrated toward the largest and brightest galaxies: e.g., M87, M49, M60–M59, and M86 (see also Liu et al. 2015a).
2. The UCDs, as a population, have bimodal color distributions. The fraction of UCDs belonging to the blue population is 89% ± 3%. This is slightly higher than that of `bright GCs` (84% ± 1% for NGVS GCs and 77% ± 4% for `ACSVCS GCs`) and slightly smaller than that of `bright nuclei` (95%).
3. We measure the mean half-light radius for UCDs to be 19.8 ± 6.8 pc. The blue UCDs (20.0 ± 6.8 pc) are systematically larger than their red counterparts (14.6 ± 3.8 pc). The largest UCD candidate in our sample is NGVS-UCD 769 with $r_h = 58.0$ pc.
4. Based on our analysis (i.e., number density maps and color distributions), we find no dramatic differences between UCDs and the brightest GCs (i.e., those objects with $g_0 < 21.5$ mag). However, when we rely on the cleanest possible UCD sample (with reduced contamination from GCs), some differences begin to appear (i.e., in their cumulative radial distributions and color–magnitude relations).
5. We identify a number of UCDs having properties that point to a connection with the nuclei of dwarf galaxies.

This includes the most luminous and largest UCDs, UCDs with obvious stellar envelopes, and UCDs embedded in diffuse asymmetric structures.

6. There are tight color–magnitude relations for UCDs and dwarf nuclei, with brighter objects being redder. At the faint end, UCDs and nuclei are bluer and have a narrower color range than GCs.

Some obvious extensions of this work present themselves, most of which involve spectroscopic observations, e.g., the property of envelopes of UCDs, searching for SMBHs in massive UCDs, and the specific frequencies for the UCDs around massive galaxies. Our radial velocity survey for UCD candidates brighter than $g_0 \sim 19.5$ mag is complete, allowing membership to be established for candidates brighter than $M_g \sim -12$, which corresponds to a stellar mass of $\sim 10^{6.9} M_\odot$ (Bell et al. 2003). It will be valuable to extend this work to the limit of our photometric catalog ($g \sim 21.5$ mag) and thus obtain a complete sample of UCDs down to a stellar mass of $\sim 10^{6.1} M_\odot$. AO-assisted IFU spectroscopy for select UCDs (i.e., the brightest and largest objects, or those objects embedded in stellar envelopes) will allow the detection of SMBHs in these objects and provide a first glimpse into the SMBH occupation fraction in a magnitude-limited UCD sample. Finally, while the NGVS has made it possible to identify UCDs larger than $r_h \sim 11$ pc throughout the Virgo cluster, space-quality imaging will be needed to extend this work to the smaller radii and fainter magnitudes typical of GCs; in the future, high-resolution imaging from the Euclid or Roman space telescopes will allow the GC/UCD size–magnitude relation(s) to be mapped roughly to the level of the GCLF turnover using spatially complete samples and unbiased structural measurements.

The NGVS team owes a debt of gratitude to the director and the staff of the Canada–France–Hawaii Telescope who helped make the survey a reality. This work is based on observations obtained with MegaPrime/MegaCam, a joint project of CFHT and CEA/DAPNIA, at the Canada–France–Hawaii Telescope (CFHT), which is operated by the National Research Council (NRC) of Canada, the Institut National des Sciences de Univers of the Centre National de la Recherche Scientifique (CNRS) of France, and the University of Hawaii. This work is based in part on data products produced at Terapix available at the Canadian Astronomy Data Centre as part of the Canada–France–Hawaii Telescope Legacy Survey, a collaborative project of NRC and CNRS.

C.L. acknowledges support from the National Natural Science Foundation of China (NSFC, grant Nos. 11673017, 11833005, 11933003, 11621303, 11973033, and 11203017). C.L. is supported by Key Laboratory for Particle Physics, Astrophysics and Cosmology, Ministry of Education, and Shanghai Key Laboratory for Particle Physics and Cosmology (SKLPPC). This work is supported by 111 project No. B20019. E.W.P. acknowledges support from the National Natural Science Foundation of China through grant No. 11573002. H.X.Z. acknowledges support from the CAS Pioneer Hundred Talents Program and the National Natural Science Foundation of China (NSFC, grant Nos. 11421303, 11973039). A.L. acknowledges support from the French Centre National d'Etudes Spatiales (CNES). E.W.P. thanks Karina Voggel for discussions in which she suggested the use of Gaia data in UCD selection.

This work was supported in part by the Sino-French LIA-Origins joint exchange program, by the French Agence Nationale de la Recherche (ANR) Grant Programme Blanc VIRAGE (ANR10-BLANC-0506-01), and by the Canadian Advanced Network for Astronomical Research (CANFAR), which has been made possible by funding from CANARIE under the Network-Enabled Platforms program. This research used the facilities of the Canadian Astronomy Data Centre operated by the National Research Council of Canada with the support of the Canadian Space Agency. This research has made use of the NASA/IPAC Extragalactic Database (NED), which is funded by the National Aeronautics and Space Administration and operated by the California Institute of Technology. This research has made use of the SIMBAD database, operated at CDS, Strasbourg, France. This publication has made use of data products from the Sloan Digital Sky Survey (SDSS). Funding for SDSS and SDSS-II has been provided by the Alfred P. Sloan Foundation, the Participating Institutions, the National Science Foundation, the U.S. Department of Energy, the National Aeronautics and Space Administration, the Japanese Monbukagakusho, the Max Planck Society, and the Higher Education Funding Council for England. This work is based in part on data obtained as part of the UKIRT Infrared Deep Sky Survey.

This research uses data obtained through the Telescope Access Program (TAP), which has been funded by the National Astronomical Observatories, Chinese Academy of Sciences, and the Special Fund for Astronomy from the Ministry of Finance. Observations reported here were obtained at the MMT Observatory, a joint facility of the University of Arizona and the Smithsonian Institution.

Facility: CFHT—Canada–France–Hawaii Telescope.

Appendix

As described in Section 3, we use strict half-light radius criteria to select UCD candidates, including (1) a radius cut ($11 < \langle r_h \rangle < 100$ pc); (2) a requirement that the half-light radii measured in the g and i bands are in rough agreement ($|r_{h,g} - r_{h,i}|/\langle r_h \rangle \leqslant 0.5$); and (3) a condition that the fraction radius errors are smaller than 15% in both bands ($r_{h,g,\mathrm{error}}/r_{h,g} \leqslant 15\%$ and $r_{h,i,\mathrm{error}}/r_{h,i} \leqslant 15\%$). In this section, we take a closer look at objects that do not satisfy our radius criteria (but satisfy all other selection criteria). We divide such objects into three groups: objects with larger errors, objects with larger differences between two bands, and objects with smaller radius measurements.

Objects with larger errors (i.e., $r_{h,g,\mathrm{error}}/r_{h,g} > 15\%$ or/and $r_{h,i,\mathrm{error}}/r_{h,i} > 15\%$): We visually inspected the imaging for objects with larger errors for their radius measurements. Most of these objects are blends or have poor image quality (i.e., sources located close to chips gaps or near saturated objects). We cannot classify these objects as bona fide UCDs using the NGVS images alone.

Objects with larger differences (i.e., $|r_{h,g} - r_{h,i}|/\langle r_h \rangle > 0.5$): The differences in image quality (PSF) are the primary reason for the large differences in radius measurements. If an object is larger than 11 pc in both the g and i bands, then we believe it be may indeed be a UCD candidate although the radius difference between two bands is large. We list nine such objects in Table A1.

Objects with smaller radius measurements (i.e., $\langle r_h \rangle < 11$ pc): Most objects with smaller measured radii are

Table A1
The Probable UCD Candidates Not Included in the Main Sample

	ID	α_{J2000} (deg)	δ_{J2000} (deg)	g_0 (mag)	$r_{h,g}$ (pc)	$r_{h,i}$ (pc)	v_r (km s^{-1})	v_{source}
	(1)	(2)	(3)	(4)	(5)	(6)	(7)	(8)
	1	186.5656471	16.0492075	19.857 ± 0.001	17.75 ± 1.37	35.32 ± 1.70	⋯	⋯
$r_h > 11$ pc	2	185.1411400	15.8494361	21.548 ± 0.005	15.95 ± 2.05	28.76 ± 1.21	⋯	⋯
in both g	3	188.7565072	17.0687625	21.094 ± 0.003	15.13 ± 1.37	28.27 ± 0.89	⋯	⋯
and i bands	4	188.2201250	16.0768933	21.431 ± 0.006	13.32 ± 1.06	28.21 ± 1.73	⋯	⋯
but large	5	190.6792998	16.5254659	21.468 ± 0.005	11.78 ± 0.70	25.20 ± 0.76	⋯	⋯
difference	6	186.1282677	16.7516812	21.528 ± 0.004	16.96 ± 0.55	28.31 ± 1.00	⋯	⋯
between the	7	188.3270896	16.7757418	21.418 ± 0.004	11.26 ± 0.70	22.63 ± 0.60	⋯	⋯
two	8	187.8761745	17.1490799	20.986 ± 0.003	20.89 ± 0.58	12.22 ± 0.83	⋯	⋯
	9	188.7443865	17.1551750	20.584 ± 0.002	11.69 ± 0.54	24.27 ± 1.09	⋯	⋯
	1	187.2897173	12.6860435	19.596 ± 0.001	33.40 ± 0.95	0.61 ± 0.00	1159	MMT 09
	2	188.8007729	9.3776914	19.531 ± 0.001	2.84 ± 1.59	13.63 ± 1.10	1406	AAT 12
Candidates	3	187.7426763	11.9746280	20.694 ± 0.002	10.76 ± 0.40	10.09 ± 0.49	1230	MMT 09
with visible	4	187.1924549	13.7198340	19.743 ± 0.001	11.69 ± 1.04	9.75 ± 0.65	1022	AAT 12
envelopes	5	188.3663498	10.6465580	20.490 ± 0.002	9.95 ± 0.24	11.13 ± 0.45	⋯	⋯
	6	187.6404154	10.3641505	19.421 ± 0.001	10.45 ± 0.31	7.80 ± 0.43	143	MMT 09,AAT 12
	7	187.1115755	13.0907153	19.996 ± 0.001	10.06 ± 0.31	8.54 ± 0.33	1040	MMT 09,AAT 12
	8	187.4479438	9.8971556	20.915 ± 0.002	10.16 ± 0.55	8.44 ± 0.40	⋯	⋯

Note. (1) Object ID number, (2) R.A., (3) decl., (4) aperture-corrected g magnitude within a 3″ diameter aperture, (5) half-light radius in the g band, (6) half-light radius in the i band, (7) radial velocity, and (8) the source of velocity measurement—AAT 12: AAT 2012 program; MMT 09: MMT 2009 program (Ferrarese et al. 2012).

likely to be GCs. However, if they have visible envelopes, then they are viable UCD candidates. We find eight objects that have half-light radii slightly below our $r_h = 11$ pc limit but appear to show diffuse envelopes. These are listed in Table A1.

To ensure our samples are as homogeneous as possible, we have not used these 17 UCD candidates in our analysis but they are included here for completeness.

ORCID iDs

Chengze Liu https://orcid.org/0000-0002-4718-3428
Patrick Côté https://orcid.org/0000-0003-1184-8114
Eric W. Peng https://orcid.org/0000-0002-2073-2781
Joel Roediger https://orcid.org/0000-0002-0363-4266
Hongxin Zhang https://orcid.org/0000-0003-1632-2541
Laura Ferrarese https://orcid.org/0000-0002-8224-1128
Ruben Sánchez-Janssen https://orcid.org/0000-0003-4945-0056
Puragra Guhathakurta https://orcid.org/0000-0001-8867-4234
Xiaohu Yang https://orcid.org/0000-0003-3997-4606
Yipeng Jing https://orcid.org/0000-0002-4534-3125
Karla Alamo-Martínez https://orcid.org/0000-0002-5897-7813
John P. Blakeslee https://orcid.org/0000-0002-5213-3548
Alessandro Boselli https://orcid.org/0000-0002-9795-6433
Pierre-Alain Duc https://orcid.org/0000-0003-3343-6284
Patrick Durrell https://orcid.org/0000-0001-9427-3373
Andres Jordán https://orcid.org/0000-0002-5389-3944
Youkyung Ko https://orcid.org/0000-0001-6333-599X
Ariane Lançon https://orcid.org/0000-0002-7214-8296
Sungsoon Lim https://orcid.org/0000-0002-5049-4390
Alessia Longobardi https://orcid.org/0000-0001-5569-6584
Simona Mei https://orcid.org/0000-0002-2849-559X
J. Christopher Mihos https://orcid.org/0000-0002-7089-8616
Roberto Muñoz https://orcid.org/0000-0003-1743-0456
Mathieu Powalka https://orcid.org/0000-0002-1218-3276
Thomas Puzia https://orcid.org/0000-0003-0350-7061
Chelsea Spengler https://orcid.org/0000-0002-1685-4284
Elisa Toloba https://orcid.org/0000-0001-6443-5570

References

Abolfathi, B., Aguado, D. S., Aguilar, G., et al. 2018, ApJS, 235, 42
Afanasiev, A. V., Chilingarian, I. V., Mieske, S., et al. 2018, MNRAS, 477, 4856
Ahn, C. P., Seth, A. C., Cappellari, M., et al. 2018, ApJ, 858, 102
Ahn, C. P., Seth, A. C., den Brok, M., et al. 2017, ApJ, 839, 72
Bekki, K., Couch, W. J., & Drinkwater, M. J. 2001, ApJL, 552, L105
Bekki, K., Couch, W. J., Drinkwater, M. J., & Shioya, Y. 2003, MNRAS, 344, 399
Bekki, K., & Freeman, K. C. 2003, MNRAS, 346, L11
Bekki, K., & Yong, D. 2012, MNRAS, 419, 2063
Bell, E. F., McIntosh, D. H., Katz, N., & Weinberg, M. D. 2003, ApJS, 149, 289
Bellazzini, M., Ibata, R. A., Chapman, S. C., et al. 2008, AJ, 136, 1147
Bertin, E., & Arnouts, S. 1996, A&AS, 117, 393
Binggeli, B., Sandage, A., & Tammann, G. A. 1985, AJ, 90, 1681
Blakeslee, J. P., & Barber DeGraaff, R. 2008, AJ, 136, 2295
Blakeslee, J. P., Jordán, A., Mei, S., et al. 2009, ApJ, 694, 556
Blom, C., Forbes, D. A., Foster, C., Romanowsky, A. J., & Brodie, J. P. 2014, MNRAS, 439, 2420
Böhringer, H., Briel, U. G., Schwarz, R. A., et al. 1994, Natur, 368, 828
Boselli, A., Fossati, M., Ferrarese, L., et al. 2018, A&A, 614, A56
Boselli, A., Voyer, E., Boissier, S., et al. 2014, A&A, 570, A69
Brinchmann, J., Kunth, D., & Durret, F. 2008, A&A, 485, 657
Brodie, J. P., Romanowsky, A. J., Strader, J., & Forbes, D. A. 2011, AJ, 142, 199
Cantiello, M., Blakeslee, J. P., Ferrarese, L., et al. 2018, ApJ, 856, 126
Chiboucas, K., Tully, R. B., Marzke, R. O., et al. 2011, ApJ, 737, 86
Chilingarian, I. V., & Mamon, G. A. 2008, MNRAS, 385, L83
Côté, P., Blakeslee, J. P., Ferrarese, L., et al. 2004, ApJS, 153, 223
Côté, P., McLaughlin, D. E., Cohen, J. G., & Blakeslee, J. P. 2003, ApJ, 591, 850
Côté, P., Piatek, S., Ferrarese, L., et al. 2006, ApJS, 165, 57
Crain, R. A., Schaye, J., Bower, R. G., et al. 2015, MNRAS, 450, 1937
Da Costa, G. S., Grebel, E. K., Jerjen, H., Rejkuba, M., & Sharina, M. E. 2009, AJ, 137, 4361
Da Rocha, C., Mieske, S., Georgiev, I. Y., et al. 2011, A&A, 525, A86

Dabringhausen, J., Kroupa, P., Pflamm-Altenburg, J., & Mieske, S. 2012, ApJ, 747, 72
De Bórtoli, B. J., Bassino, L. P., Caso, J. P., & Ennis, A. I. 2020, MNRAS, 492, 4313
Drinkwater, M., Bekki, K., Couch, W., et al. 2002, in IAU Symp. 207, Extragalactic Star Clusters, ed. D. P. Geisler, E. K. Grebel, & D. Minniti (San Francisco, CA: ASP), 287
Drinkwater, M. J., Gregg, M. D., Couch, W. J., et al. 2004, PASA, 21, 375
Drinkwater, M. J., Gregg, M. D., Hilker, M., et al. 2003, Natur, 423, 519
Drinkwater, M. J., Jones, J. B., Gregg, M. D., & Phillipps, S. 2000, PASA, 17, 227
Durrell, P. R., Côté, P., Peng, E. W., et al. 2014, ApJ, 794, 103
Evans, D. W., Riello, M., De Angeli, F., et al. 2018, A&A, 616, A4
Evstigneeva, E. A., Drinkwater, M. J., Jurek, R., et al. 2007a, MNRAS, 378, 1036
Evstigneeva, E. A., Gregg, M. D., Drinkwater, M. J., & Hilker, M. 2007b, AJ, 133, 1722
Fahrion, K., Georgiev, I., Hilker, M., et al. 2019, A&A, 625, A50
Faifer, F. R., Escudero, C. G., Scalia, M. C., et al. 2017, A&A, 599, L8
Fasano, G., & Franceschini, A. 1987, MNRAS, 225, 155
Fellhauer, M., & Kroupa, P. 2002, MNRAS, 330, 642
Ferrarese, L., Côté, P., Cuillandre, J.-C., et al. 2012, ApJS, 200, 4
Ferrarese, L., Côté, P., Jordán, A., et al. 2006, ApJS, 164, 334
Ferrarese, L., Côté, P., MacArthur, L. A., et al. 2020, ApJ, 890, 128
Ferrarese, L., Côté, P., Sánchez-Janssen, R., et al. 2016, ApJ, 824, 10
Forbes, D. A., Alabi, A., Brodie, J. P., et al. 2017, AJ, 153, 114
Forbes, D. A., Norris, M. A., Strader, J., et al. 2014, MNRAS, 444, 2993
Gebhardt, K., & Kissler-Patig, M. 1999, AJ, 118, 1526
Gratton, R., Bragaglia, A., Carretta, E., et al. 2019, A&ARv, 27, 8
Guérou, A., Emsellem, E., McDermid, R. M., et al. 2015, ApJ, 804, 70
Guo, Q., White, S., Boylan-Kolchin, M., et al. 2011, MNRAS, 413, 101
Haşegan, M., Jordán, A., Côté, P., et al. 2005, ApJ, 627, 203
Hanes, D. A., Côté, P., Bridges, T. J., et al. 2001, ApJ, 559, 812
Hilker, M. 2006, arXiv:0605.447
Hilker, M. 2011, EAS Publ. Ser., 48, 219
Hilker, M., Infante, L., Vieira, G., Kissler-Patig, M., & Richtler, T. 1999, A&AS, 134, 75
Huxor, A. P., Mackey, A. D., Ferguson, A. M. N., et al. 2014, MNRAS, 442, 2165
Huxor, A. P., Tanvir, N. R., Irwin, M. J., et al. 2005, MNRAS, 360, 1007
Hwang, N., & Lee, M. G. 2008, AJ, 135, 1567
Hwang, N., Lee, M. G., Lee, J. C., et al. 2011, ApJ, 738, 58
Ibata, R. A., Bellazzini, M., Malhan, K., Martin, N., & Bianchini, P. 2019, NatAs, 3, 667
Ibata, R. A., Gilmore, G., & Irwin, M. J. 1994, Natur, 370, 194
Janz, J., Forbes, D. A., Norris, M. A., et al. 2015, MNRAS, 449, 1716
Janz, J., Norris, M. A., Forbes, D. A., et al. 2016, MNRAS, 456, 617
Jennings, Z. G., Romanowsky, A. J., Brodie, J. P., et al. 2015, ApJL, 812, L10
Jennings, Z. G., Strader, J., Romanowsky, A. J., et al. 2014, AJ, 148, 32
Johnson, C. I., Rich, R. M., Pilachowski, C. A., et al. 2015, AJ, 150, 63
Jones, J. B., Drinkwater, M. J., Jurek, R., et al. 2006, AJ, 131, 312
Jordán, A., Côté, P., Blakeslee, J. P., et al. 2005, ApJ, 634, 1002
Jordán, A., McLaughlin, D. E., Côté, P., et al. 2007, ApJS, 171, 101
Jordán, A., Peng, E. W., Blakeslee, J. P., et al. 2009, ApJS, 180, 54
Katz, D., Sartoretti, P., Cropper, M., et al. 2019, A&A, 622, A205
Ko, Y., Hwang, H. S., Lee, M. G., et al. 2017, ApJ, 835, 212
Kundu, A., & Whitmore, B. C. 2001, AJ, 121, 2950
Küpper, A. H. W., Balbinot, E., Bonaca, A., et al. 2015, ApJ, 803, 80
Küpper, A. H. W., Kroupa, P., Baumgardt, H., & Heggie, D. C. 2010, MNRAS, 401, 105
Kuzma, P. B., Da Costa, G. S., & Mackey, A. D. 2018, MNRAS, 473, 2881
Kuzma, P. B., Da Costa, G. S., Mackey, A. D., & Roderick, T. A. 2016, MNRAS, 461, 3639
Lawrence, A., Warren, S. J., Almaini, O., et al. 2007, MNRAS, 379, 1599
Li, B., Peng, E. W., Zhang, H.-x., et al. 2015, ApJ, 806, 133
Liu, C., Peng, E. W., Côté, P., et al. 2015a, ApJ, 812, 34
Liu, C., Peng, E. W., Toloba, E., et al. 2015b, ApJL, 812, L2
Liu, Y., Peng, E. W., Lim, S., et al. 2016, ApJ, 830, 99
Longobardi, A., Peng, E. W., Côté, P., et al. 2018, ApJ, 864, 36
Madrid, J. P. 2011, ApJL, 737, L13
Madrid, J. P., Graham, A. W., Harris, W. E., et al. 2010, ApJ, 722, 1707
Majewski, S. R., Skrutskie, M. F., Weinberg, M. D., & Ostheimer, J. C. 2003, ApJ, 599, 1082
Mei, S., Blakeslee, J. P., Côté, P., et al. 2007, ApJ, 655, 144
Mieske, S., Hilker, M., & Infante, L. 2002, A&A, 383, 823
Mieske, S., Hilker, M., & Infante, L. 2004a, A&A, 418, 445
Mieske, S., Hilker, M., Infante, L., & Jordán, A. 2006, AJ, 131, 2442
Mieske, S., Hilker, M., Jordán, A., Infante, L., & Kissler-Patig, M. 2007a, A&A, 472, 111
Mieske, S., Hilker, M., & Misgeld, I. 2012, A&A, 537, A3
Mieske, S., Infante, L., Benítez, N., et al. 2004b, AJ, 128, 1529
Mieske, S., Infante, L., Hilker, M., et al. 2005, A&A, 430, L25
Mieske, S., West, M. J., & de Oliveira, C. M. 2007b, in Groups of Galaxies in the Nearby Universe, ed. I. Saviane, V. D. Ivanov, & J. Borissova (Berlin: Springer), 103
Mihos, J. C., Durrell, P. R., Ferrarese, L., et al. 2015, ApJL, 809, L21
Milone, A. P., Piotto, G., Renzini, A., et al. 2017, MNRAS, 464, 3636
Muñoz, R. P., Puzia, T. H., Lançon, A., et al. 2014, ApJS, 210, 4
Muratov, A. L., & Gnedin, O. Y. 2010, ApJ, 718, 1266
Norris, M. A., & Kannappan, S. J. 2011, MNRAS, 414, 739
Norris, M. A., Kannappan, S. J., Forbes, D. A., et al. 2014, MNRAS, 443, 1151
Odenkirchen, M., Grebel, E. K., Rockosi, C. M., et al. 2001, ApJL, 548, L165
Park, H. S., Lee, M. G., & Hwang, H. S. 2012, ApJ, 757, 184
Paudel, S., Lisker, T., & Janz, J. 2010, ApJL, 724, L64
Peacock, J. A. 1983, MNRAS, 202, 615
Peng, E. W., Côté, P., Jordán, A., et al. 2006a, ApJ, 639, 838
Peng, E. W., Jordán, A., Côté, P., et al. 2006b, ApJ, 639, 95
Penny, S. J., Forbes, D. A., & Conselice, C. J. 2012, MNRAS, 422, 885
Penny, S. J., Forbes, D. A., Strader, J., et al. 2014, MNRAS, 439, 3808
Pfeffer, J., & Baumgardt, H. 2013, MNRAS, 433, 1997
Pfeffer, J., Griffen, B. F., Baumgardt, H., & Hilker, M. 2014, MNRAS, 444, 3670
Pfeffer, J., Hilker, M., Baumgardt, H., & Griffen, B. F. 2016, MNRAS, 458, 2492
Phillipps, S., Drinkwater, M. J., Gregg, M. D., & Jones, J. B. 2001, ApJ, 560, 201
Pota, V., Brodie, J. P., Bridges, T., et al. 2015, MNRAS, 450, 1962
Pota, V., Forbes, D. A., Romanowsky, A. J., et al. 2013, MNRAS, 428, 389
Powalka, M., Lançon, A., Puzia, T. H., et al. 2016a, ApJS, 227, 12
Powalka, M., Puzia, T. H., Lançon, A., et al. 2016b, ApJL, 829, L5
Riello, M., De Angeli, F., Evans, D. W., et al. 2018, A&A, 616, A3
Roediger, J. C., Ferrarese, L., Côté, P., et al. 2017, ApJ, 836, 120
Sánchez-Janssen, R., Côté, P., Ferrarese, L., et al. 2019, ApJ, 878, 18
Sánchez-Janssen, R., Ferrarese, L., MacArthur, L. A., et al. 2016, ApJ, 820, 69
Sandoval, M. A., Vo, R. P., Romanowsky, A. J., et al. 2015, ApJL, 808, L32
Schlegel, D. J., Finkbeiner, D. P., & Davis, M. 1998, ApJ, 500, 525
Schweizer, F., Seitzer, P., Whitmore, B. C., Kelson, D. D., & Villanueva, E. V. 2018, ApJ, 853, 54
Seth, A. C., van den Bosch, R., Mieske, S., et al. 2014, Natur, 513, 398
Spengler, C., Côté, P., Roediger, J., et al. 2017, ApJ, 849, 55
Strader, J., Fabbiano, G., Luo, B., et al. 2012, ApJ, 760, 87
Strader, J., Romanowsky, A. J., Brodie, J. P., et al. 2011, ApJS, 197, 33
Strader, J., Seth, A. C., Forbes, D. A., et al. 2013, ApJL, 775, L6
Toloba, E., Li, B., Guhathakurta, P., et al. 2016, ApJ, 822, 51
Toloba, E., Lim, S., Peng, E., et al. 2018, ApJL, 856, L31
van den Bergh, S., & Mackey, A. D. 2004, MNRAS, 354, 713
van den Bergh, S., Morbey, C., & Pazder, J. 1991, ApJ, 375, 594
Villegas, D., Jordán, A., Peng, E. W., et al. 2010, ApJ, 717, 603
Voggel, K., Hilker, M., & Richtler, T. 2016, A&A, 586, A102
Voggel, K. T., Seth, A. C., Sand, D. J., et al. 2020, ApJ, 899, 140
Wehner, E. M. H., & Harris, W. E. 2007, ApJL, 668, L35
Wenger, M., Ochsenbein, F., Egret, D., et al. 2000, A&AS, 143, 9
Willman, B., & Strader, J. 2012, AJ, 144, 76
Zhang, H.-X., Peng, E. W., Côté, P., et al. 2015, ApJ, 802, 30
Zhang, H.-X., Puzia, T. H., Peng, E. W., et al. 2018, ApJ, 858, 37